

HIGH-RESOLUTION, WIDE-FIELD IMAGING OF THE GALACTIC CENTER REGION AT 330 MHz

MICHAEL E. NORD,¹ T. JOSEPH W. LAZIO, AND NAMIR E. KASSIM

Remote Sensing Division, Code 7213, Naval Research Laboratory, 4555 Overlook Avenue, SW, Washington, DC 20375-5351;
Michael.Nord@nrl.navy.mil, Joseph.Lazio@nrl.navy.mil, Namir.Kassim@nrl.navy.mil

S. D. HYMAN

Department of Physics and Engineering, Sweet Briar College, Sweet Briar, VA 24595; shyman@sbc.edu

T. N. LAROSA

Department of Biological and Physical Sciences, Kennesaw State University, 1000 Chastain Road,
Kennesaw, GA 30144; ted@avatar.kennesaw.edu

C. L. BROGAN

Institute for Astronomy, 640 North A'ohoku Place, Hilo, HI 96720; cbrogan@ifa.hawaii.edu

AND

N. DURIC

Department of Physics and Astronomy, University of New Mexico,
800 Yale Boulevard, NE, Albuquerque, NM 87131;
duric@tesla.phys.unm.edu

Received 2004 June 4; accepted 2004 July 8

ABSTRACT

We present a wide-field, subarcminute-resolution VLA image of the Galactic center region at 330 MHz. With a resolution of $\sim 7'' \times 12''$ and an rms noise of $1.6 \text{ mJy beam}^{-1}$, this image represents a significant increase in resolution and sensitivity over the previously published VLA image at this frequency. The improved sensitivity has more than tripled the census of small-diameter sources in the region, has resulted in the detection of two new nonthermal filaments (NTFs), 18 NTF candidates, and 30 pulsar candidates, reveals previously known extended sources in greater detail, and has resulted in the first detection of Sagittarius A* in this frequency range.

Key words: Galaxy: center — radio continuum: general — techniques: interferometric

1. INTRODUCTION

At a distance of only 8 kpc, the Galactic center (GC) offers an unparalleled site for examining the environment of a (moderately) active galactic nucleus. A multiwavelength approach is essential to understanding the diverse range of phenomena in the GC, and low frequencies ($\nu < 1000 \text{ MHz}$) provide several crucial benefits in obtaining a complete picture of the GC. At 330 MHz, thermal sources such as classical H II regions have not yet become self-absorbed, while nonthermal sources such as supernova remnants (SNRs) are typically detected easily. Thus the interactions between these sources (e.g., in regions of massive star formation) can be studied. More generally, low-frequency observations have intrinsically large fields of view, allowing the various components of the GC to be placed into a larger context.

The Galactic center was first imaged at 330 MHz at high resolution in 1989 (Pedlar et al. 1989; Anantharamaiah et al. 1991). Advances enabled by these early imaging programs include revealing the $7'$ radio halo around the Sagittarius A region and constraining the three-dimensional structure of the region through optical depth distributions. However, imaging algorithms at the time were unable to compensate for the noncoplanar nature of the VLA. Hence, the full primary beam of the VLA at 330 MHz (FWHM $156'$) was not correctly imaged and only the very center of the GC region was studied at high fidelity.

More recently, exploiting a number of advances in imaging algorithms to compensate for the noncoplanar nature of the VLA, LaRosa et al. (2000) reimaged these data, forming a full-field-of-view image. This led to the discovery of many new sources and provided an unparalleled census of both extended and small-diameter, thermal and nonthermal sources within 100 pc (projection) of the GC. This was afforded by significant advances in wide-field imaging algorithms, coupled with greatly increased computational power. However, even that effort fell short of utilizing the full resolving power of the VLA and the commensurate improved sensitivity it would have afforded. Since those data were presented, significant improvements in software, hardware, and computational power have continued to be realized. This motivated us to revisit the GC in order to achieve further improvements in resolution and sensitivity at 330 MHz.

In this paper, we present analysis of our latest 330 MHz image generated from new A- and B-configuration data sets, which are appropriate for generating a map with a minimum of confusion noise and maximum sensitivity to smaller scale ($\lesssim 1'$) structure. Consequently the entire GC region contained by the primary beam of the VLA has been imaged at the maximum possible resolution for the first time. The image is centered on the radio-bright Sgr A region and provides a resolution of $7'' \times 12''$ and an rms sensitivity of $1.6 \text{ mJy beam}^{-1}$, an improvement by roughly a factor of 5 in both parameters over the LaRosa et al. (2000) image.

The improved sensitivity and resolution have led to the detection of at least two new nonthermal filaments (NTFs),

¹ Doctoral student, Department of Physics, University of New Mexico.

TABLE 1
OBSERVATIONAL SUMMARY

Date	Configuration	ν (MHz)	$\Delta\nu$ (MHz)	Integration (hr)	Beam (arcsec)
1996 Oct 24	A	332.5	6	5.55	9×5
1998 Mar 4	A	327.5	3	5.38	9×5
1998 Sep 26	B	327.5	3	5.47	36×20

18 NTF candidates, and 30 pulsar candidates. It has also revealed previously known extended sources in greater detail and significantly increased the census of small-diameter sources in the GC region. In § 2, we describe the observations, and in § 3 we describe data reduction, image reconstruction, and astrometry. In §§ 4 and 5, we discuss small-diameter sources, and in § 6 we present images of resolved sources including newly discovered NTFs and NTF candidates. Our conclusions are presented in § 7.

2. OBSERVATIONS

Two sets of observations were obtained, as summarized in Table 1. The first was observed at 330 MHz in the A configuration of the VLA in 1996 October. Six megahertz of total bandwidth centered on 332.5 MHz was split into 64 channels in order to enable radio-frequency interference (RFI) excision, as well as to mitigate the effects of bandwidth smearing (chromatic aberration). These data were from a series of observations designed to find candidate GC pulsars (i.e., small-diameter, steep-spectrum objects; Lazio & Cordes 2004). The second set of observations were obtained in the A and B configurations of the VLA and were obtained between 1998 March and 1999 May. A total bandwidth of 3 MHz centered at 327.5 MHz was split into 32 channels. Unlike the archival data reprocessed by LaRosa et al. (2000), all these new data were obtained using all 27 antennas of the VLA.

3. DATA REDUCTION

Data reduction and imaging at 330 MHz with the VLA utilizes procedures similar to those employed at centimeter wavelengths. Key differences are the need for more intensive data editing and the requirement to implement noncoplanar imaging of the full field of view in order to mitigate the confusion from the numerous extended and small-diameter sources in the primary beam.² In general we followed reduction and imaging procedures analogous to the steps reported in LaRosa et al. (2000), although the speed and sophistication of many of the specialized algorithms have been greatly improved.

Initial flux density and phase calibration were conducted in the standard manner, with Cygnus A used for bandpass calibration in the 1998 data and 3C 286 used in the 1996 data. Flux density calibration was based on observations of 3C 286, and initial phase calibration was obtained using the VLA calibrators B1830–360 and B1711–251.

3.1. Radio-Frequency Interference Excision

A key issue for low-frequency data reduction at the VLA is the impact of RFI. Some sources of interference, such as lightning and solar-related activity, are normally broadband and require those time periods to be completely excised from

the data. However, RFI at 330 MHz is mostly narrowband. Algorithms exist that attempt to automate the removal of only those channels with interference. We elected to inspect the data and remove RFI manually because in our experiences with automated RFI excision, available algorithms either removed too much good data or failed to excise sufficient RFI, particularly at low levels.

RFI excision was based on the following criteria: First, visibilities with excessive amplitudes (e.g., above 100σ) were flagged. Then the visibility data amplitudes were scrutinized in both Stokes I and V . Stokes V is particularly useful in locating RFI, as there should be very little circular polarization at these frequencies,³ while RFI is often highly circularly polarized. Baselines and time ranges that showed excessive deviation from surrounding data were flagged. An additional means by which RFI was localized was the identification of systemic ripples in the image. Determining the spatial frequency of these ripples allowed the offending baseline and time range to be located and removed from the visibility (u - v) data set.

After RFI excision, the spectral line data were smoothed by a factor of 2 in order to lower the computational cost of imaging. As sensitivity declines steeply near the edge of the bandwidth, the end channels were omitted. The resulting data set had a bandwidth of 2.34 MHz, 12 channels with 0.195 MHz each.

3.2. Wide-Field Imaging and Self-Calibration

An additional complication for low-frequency imaging is that the combination of the large field of view (FWHM $156'$ at 330 MHz), high angular resolution, and noncoplanar nature of the VLA necessitates specialized imaging algorithms to avoid image distortion. We employed the polyhedron algorithm of Cornwell & Perley (1992), in which the sky is approximated by many two-dimensional facets. We chose our facets to be $\sim 30'$ in size. This choice was driven by the degree of noncoplanar image distortion deemed acceptable at facet edges. The algorithm shifts the phase center to the center of an individual facet and then grids the u - v channel data before it is imaged. Iterating over many facets allows the entire primary beam to be imaged with minimal noncoplanar effects, at the minimal bandwidth smearing of the individual channels, and at the sensitivity of the full bandwidth.

Below ~ 1 GHz, atmospheric phase errors for interferometers are dominated by the ionosphere. In order to remove ionospheric phase errors, an imaging/self-calibration (Cornwell & Fomalont 1999) loop is used. For each data set, several iterations of self-calibration were used to improve the dynamic range. A phase self-calibration interval of 2 minutes was used, as this is generally short enough to track ionospheric changes and long enough to provide a sufficient signal-to-noise ratio. Amplitude self-calibration was used only after many iterations of phase-only imaging/self-calibration loops and utilized larger solution intervals, as described below.

Current angle-invariant implementations of self-calibration solve for one phase and/or amplitude per antenna per time interval. For this reason, only ionospheric fluctuations with isoplanatic patch sizes on the sky large compared with the field of view can be properly removed. Forms of angle-variant

² A full description of low-frequency VLA data reduction procedures is at <http://rsd-www.nrl.navy.mil/7213/lazio/tutorial/>.

³ The radio source associated with the massive black hole in the center of our galaxy, Sgr A*, is slightly circularly polarized at higher frequencies (Bower et al. 1999). However, the flux density of this source is very low ($<0.1\%$) compared with the total flux density in the field.

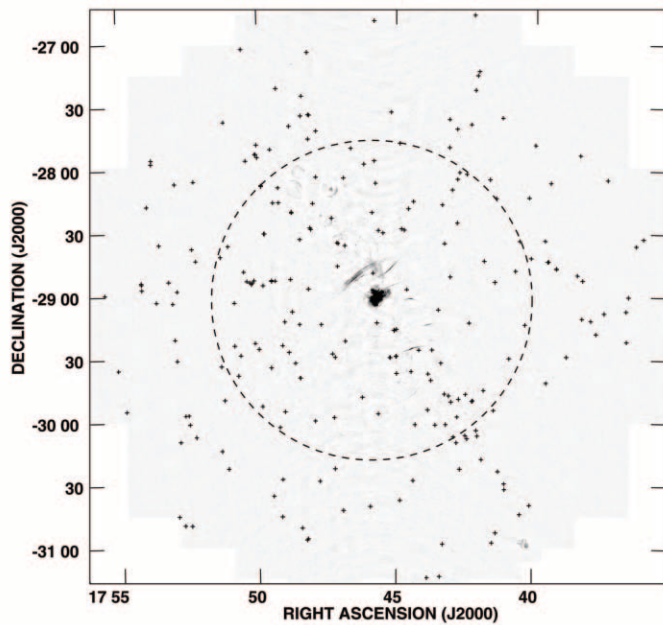


FIG. 1.—The 330 MHz A- plus B-configuration image of the Galactic center region. Primary-beam correction has not been applied. The dashed circle represents the half-power point of the primary beam (FWHM $\sim 156'$). The synthesized beam is $12'' \times 7''$, and the rms noise is $1.6 \text{ mJy beam}^{-1}$. The gray scale is linear between -2 and 50 mJy beam^{-1} . The scalloping of the image around the edges delimits the region imaged. Plus signs indicate the locations of small-diameter sources from Table 2.

self-calibration are needed to compensate for nonisoplanatic effects, especially at the lower VLA frequency of 74 MHz where those effects become severe.

The state of ionospheric weather during an observation has a strong bearing on data quality. We were fortunate to have a very calm ionosphere during both A-configuration observations. In our B-configuration observation, the ionosphere was less calm and data from a small number of relatively longer $u-v$ baselines had to be flagged for the first 2 hours of the observation. However, those data were compensated for by high-quality A-configuration data covering regions of the $u-v$ plane lost to the turbulent ionospheric conditions early in the B configuration.

For the special case of the GC, most ($>90\%$) of the flux density in the primary beam lies within the central facet containing Sgr A. Until properly deconvolved, artifacts from Sgr A dominate all other sources of error in the image. At the early stages of imaging, calibration and ionospheric phase errors compound this confusion problem. Therefore, in the first imaging iteration, only the central facet containing Sgr A was imaged. However, much of the emission in this field is diffuse, and standard deconvolution, which assumes point sources on an empty background, will not deconvolve this diffuse emission effectively. Hence, SDI deconvolution (Steer et al. 1984) in AIPS was used. SDI Clean more effectively cleans diffuse emission by selecting and deconvolving all pixels above a certain intensity in an image instead of iteratively deconvolving a few bright pixels. However, we found that starting with SDI Clean resulted in the removal of too much emission from the central bright region, causing deconvolution errors in each successive major cycle. Therefore, deconvolution was started with standard Cotton-Schwab (SGI) Clean and switched to SDI after the first major cycle. Gradually the number of facets was expanded so that successive

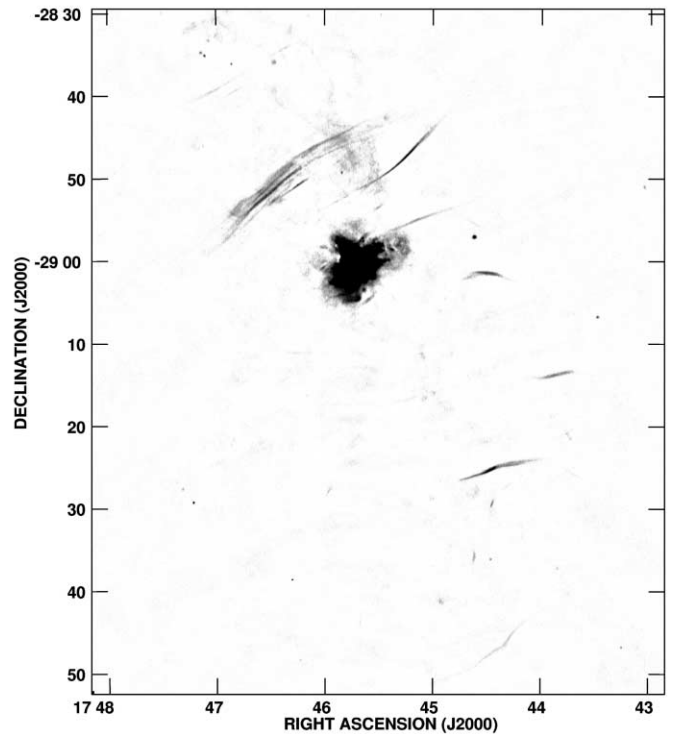


FIG. 2.—The inner $\sim 1^\circ 0' \times 1^\circ 2'$ of Fig. 1. This image was generated using a nonlinear transfer function in order to show the detail in the Sgr A region and the fainter NTFs and NTF candidates.

loops of phase self-calibration and imaging encompassed the full field of view. Once the number of facets was been expanded to include the entire field, a final amplitude and phase self-calibration with a long ($\sim 1 \text{ hr}$) solution interval was performed to correct for any systematic gain offsets between antennas.

3.3. Multiconfiguration Data Synthesis

The data from each of the three epochs were reduced separately following the procedures outlined above. Once reasonably high dynamic range images could be produced from all three data sets, intensities of small-diameter sources were checked for internal consistency. The 1996 A-configuration image was found to have small-diameter source intensities that were systematically low by a factor of roughly 20%, for reasons we could not determine. For this reason, as well as to bring all data onto a common amplitude scale, the data sets were self-calibrated one final time. The concatenated $u-v$ data set was amplitude and phase self-calibrated with the 1998 B-configuration image as the model. The self-calibration was done using a time interval of 12 hr, longer than the time of any of the individual observations. This corrected for any systemic gain or position offsets between the data sets. The B-configuration model was chosen to anchor this alignment because use of an A-configuration model would bias the flux densities to be too low. While this technique aligned the flux density scales of the three data sets, absolute flux density calibration remains unknown at about the 5% level (Baars et al. 1977). After this last self-calibration, the combined data were imaged a final time, producing the final facets. For the final image, all facets were interpolated onto one large grid, resulting in a single image with a resolution of $\sim 7'' \times 12''$ and an rms noise of $1.6 \text{ mJy beam}^{-1}$. Figure 1 shows the final image, containing over 300 million $1'' \times 1''$ pixels, and Figure 2 shows

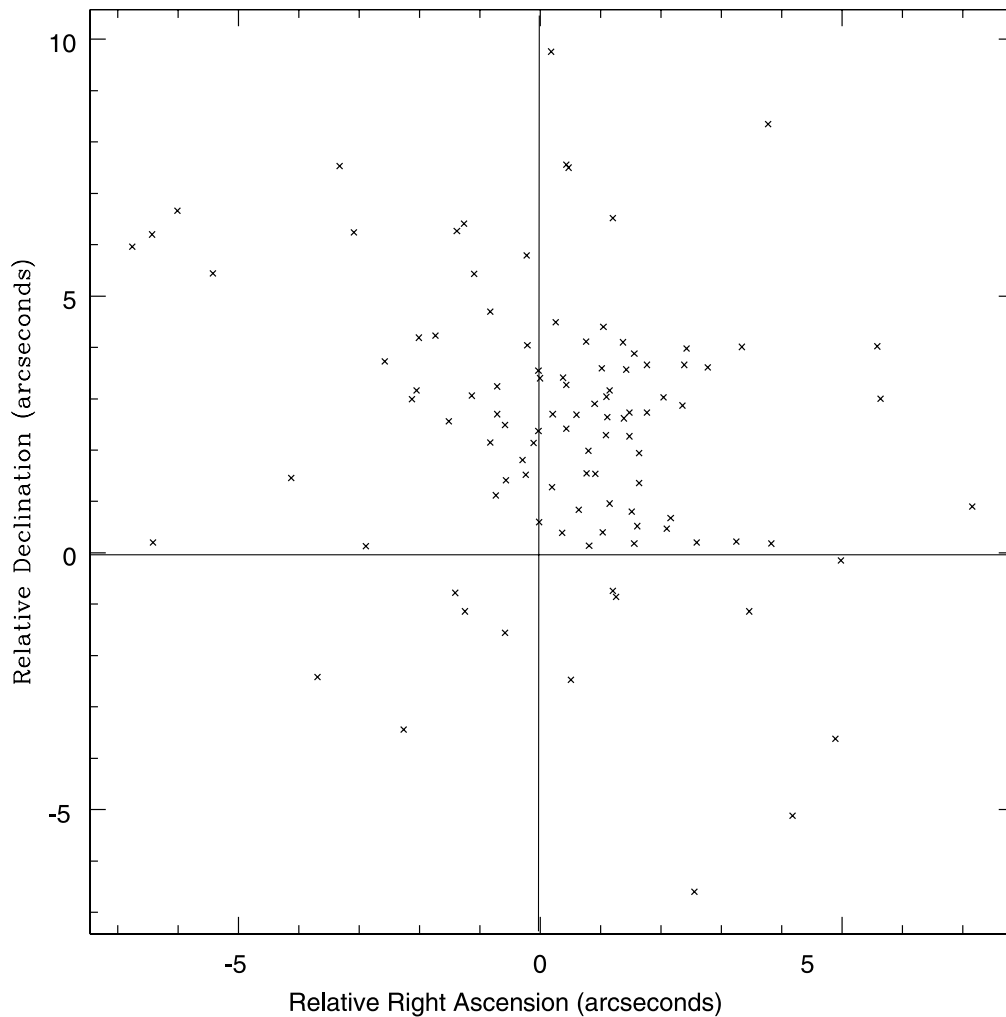


FIG. 3.—Position offset between the NVSS positions and the nominal positions for 103 small-diameter sources common to both surveys. The astrometric correction applied in § 3.4 was derived from these offsets.

the central $\sim 1.2 \times 1.0$ of the field. The total deconvolved flux density from the combined data set was 326 Jy.

3.4. Astrometry

Absolute position determination for low-frequency images inevitably relies on tying their coordinates to a grid of sources whose positions are determined from higher frequency maps. The low-frequency data alone are incapable of providing good astrometry, for two key reasons. First, self-calibration inherently returns an improved visibility data set whose position is arbitrarily tied to the position of an imperfect starting model. Secondly, even prior to self-calibration the large-scale component of the ionosphere introduces an arbitrary phase shift on both target field and phase calibrator observations. Fortunately, as described by Erickson (1984), this second effect manifests itself mainly as a global position shift and, to first order, does not distort the brightness distribution within the image. Hence, to correct for these positional inaccuracies, small-diameter sources extracted from the image (§ 4) were registered against the 1.4 GHz NRAO VLA Sky Survey (NVSS; Condon et al. 1998). Figure 3 shows the relative positions of the 103 matching sources. The mean of this distribution is offset from zero by $0''.37$ in right ascension and $2''.4$ in declination. All small-diameter source positions were adjusted to account for

these offsets. We define the rms deviation from the mean, $2''.1$, as the positional accuracy of the compact sources.

4. SMALL-DIAMETER SOURCES

Locating and cataloging small-diameter ($\lesssim 2$ beamwidths) sources in the GC region is challenging. Regions of extended emission can confuse automated small-diameter source detection algorithms, yet detection by eye can bias against finding weak sources. In this data set, we have the advantage that a great deal of the extended emission in the region has been resolved out but enough emission still exists in supernova remnants, nonthermal filaments, and extended H II regions to confuse automated searches. For this reason, we used a hybrid small-diameter source search method in which regions of extended emission were excluded from automated small-diameter source searches. These regions included the Sgr A region and the region to the northeast along the Galactic plane extending out to the Sgr D H II region. To the south, the NTF Sgr C and the “Tornado” SNR were also removed. From the remaining region, an automated small-diameter source search algorithm⁴ was used to locate sources with a signal-to-noise

⁴ AIPS task SAD.

threshold exceeding 5σ . Searches by eye were then used in areas that had been removed. Because of confusing flux density, small-diameter source detection in these areas cannot be considered complete. Finally, all sources were examined by eye to exclude genuinely extended sources, sidelobe artifacts, or similarly misidentified small-diameter sources. In total, 241 small-diameter sources were identified in this manner, more than tripling the number of small-diameter sources detected in LaRosa et al. (2000). Figure 1 shows the locations of the Galactic Center P-Band Survey (GCPS) small-diameter sources.

Once the small-diameter sources had been found, two-dimensional Gaussians were fitted to the sources in order to solve for positions, intensities, flux densities, and deconvolved sizes. The distance of each source from the phase center was computed, and the resulting primary-beam correction was applied. It should be noted that the primary-beam correction is a modeled function, and therefore flux densities of sources beyond the half-power point of the primary beam ($\sim 80'$) should be considered uncertain. Furthermore, there are many sources in the GC region that are extended at this resolution but are still detected by the search routine. For this reason, we include the average of the major and minor axes of the Gaussian fit to each source. In the cases where this value is significantly greater than the average beam size ($9''.75$), the source may be partially resolved and the flux density measurement is therefore only a lower limit. Details are given in Table 2. Column (1) numbers the sources, column (2) identifies sources using their Galactic coordinates, columns (3) and (4) give source equatorial coordinates, column (5) gives maximum intensity, column (6) gives the rms of the image in the region local to the source, column (7) gives flux density, column (8) gives the arithmetic mean of the deconvolved major and minor axes, column (9) gives the offset of the source from the phase center, and column (10) contains information pertaining to source matches from the SIMBAD database. Figure 4 displays the locations of sources in Table 2.

In order to obtain spectral information, we compared our catalog (Table 2) against three catalogs at higher frequencies. Table 3 details sources having counterparts in these surveys. Sources were considered a match if their stated location matched ours to within $15''$. At a frequency of 1.4 GHz, the GPSR (Zoonematkermani et al. 1990; Helfand et al. 1992) and 2LC (Lazio & Cordes 2004) surveys were used. The GPSR matches our observations well in survey area and in resolution. The 2LC has a much smaller beam size and limited coverage (inner $\sim 1^\circ$) but was useful in resolving sources separated by less than a beam. At 5 GHz, the companion survey to the GPSR, the GPSR5 (Becker et al. 1994), was used, as it matches our resolution and coverage as well.

Of particular note are two transient sources (GCRT J1746–2757 and XTE J1748–288), both described in Hyman et al. (2002). The former was discovered with these data and is undetected in X-rays. The latter, an X-ray transient, was first detected at higher radio frequencies by Hjellming et al. (1998). We are presently monitoring the GC at 330 MHz several times a year in order to constrain the frequency and magnitude of Galactic center transients (Hyman et al. 2003).

5. ASSESSING SMALL-DIAMETER SOURCE POPULATIONS

5.1. Small-Diameter Source Density

As the Galactic center is one of the most densely populated regions of the sky, we expect the source density to be greater

than in other regions of the sky. To test this hypothesis, source counts from the deep WSRT (Wieringa 1991) and Cohen et al. (2003) surveys, both at 330 MHz, were examined. Cohen et al. imaged a region far from the Galactic plane with the VLA with sensitivity and beam size similar to our GC image. Within the half-power point of the primary beam, and correcting for slightly greater sensitivity in the Cohen et al. image, 209 small-diameter sources were detected by Cohen et al. versus 123 in our Galactic center image. Wieringa (1991) used the Westerbork synthesis array telescope to survey a large region of the sky ($\sim 90 \text{ deg}^2$) and fitted a differential source count (dN/dS) model to the data. Figure 5 shows the Euclidian normalized differential source counts for the Galactic center image with the dN/dS model from the deep WSRT survey (Wieringa 1991) superposed. The number of sources expected under this model was obtained by numerical integration of the following:

$$N = \int_{\theta_{\min}}^{\theta_{\max}} 2\pi d\theta \int_{S_{\min}}^{\infty} \frac{dN}{dS} dS.$$

Here θ_{\min} is the radial distance from the phase center at which the integration is started, θ_{\max} is the radial distance at which the integration is stopped, and S_{\min} is the minimum detectable intensity at θ_{\max} . For our purposes, $\theta_{\min} = 10'$ in order to exclude the central Sgr A supernova remnant, θ_{\max} is the FWHM of the primary beam, and S_{\min} is 15 mJy, the 5σ detection limit at the FWHM of the primary beam. With these values, Wieringa's source-count model predicts 194 sources out to the survey limit of Cohen et al. (1.3 radius). The observed value of Cohen et al. (2003) and the expected value of Wieringa (1991) agree to within 7%. However, the GC region's 123 sources represent an underdensity of $\sim 40\%$. This is at least partly explained by the presence of bright extended sources such as Sgr A, Sgr B, and Sgr C, as detection of small-diameter sources that lie behind them is not possible. However, these sources cover no more than 5% of the region. To explain this underdensity, we hypothesize that the free electron scattering screen of Cordes & Lazio (2003) is sufficiently strong in the GC region that sources of lower intrinsic intensity are being scattered to such an extent that their surface brightness falls below the detection limit of the survey. The scattering model and the ramifications of this observation are covered in detail in § 5.3.

5.2. Small-Diameter Source Classification

At high Galactic latitudes, the field of view at 330 MHz is dominated by an extragalactic source population, typically radio galaxies (see, e.g., Cohen et al. 2003). Given that the line of sight for this observation passes through the maximum extent of the Galactic disk, we also expect a contribution from a Galactic source population or populations. In this section we assess the extent to which we have detected both a Galactic and extragalactic population of sources and, in particular, seek to classify the underlying nature of the small-diameter component.

To determine if any Galactic population is present, the clustering of sources near the Galactic plane was examined. Figure 1 shows the distribution of small-diameter sources. The sources appear to be concentrated along the Galactic plane. In order to test this observation statistically, all small-diameter sources were placed onto a radial coordinate frame. The observation (phase) center is the center of the frame, the parallel to the Galactic plane toward the north is defined as 0° , and

TABLE 2
GALACTIC CENTER P-BAND SURVEY OF SMALL-DIAMETER SOURCES

GCPS No. (1)	Name (2)	R.A. (J2000) (3)	Decl. (J2000) (4)	I (mJy beam ⁻¹) (5)	rms (mJy beam ⁻¹) (6)	S (mJy) (7)	θ (arcsec) (8)	Offset (arcmin) (9)	SIMBAD Match ^a (10)
1.....	357.796−0.790	17 43 24.22	−31 13 39.6	89.7	13.2	234.2	10.4	136.2	
2.....	357.809−0.300	17 41 29.34	−30 57 32.6	168.8	11.0	237.2	5.8	129.0	
3.....	357.841−0.881	17 43 52.51	−31 14 13.0	82.6	13.1	337.0	12.0	136.0	
4.....	357.861−0.234	17 41 21.34	−30 52 44.8	64.4	9.9	91.6	13.5	125.3	
5.....	357.866−0.997	17 44 23.82	−31 16 36.2	233.4	13.5	881.6	15.2	137.0	
6.....	357.886+0.004	17 40 28.64	−30 43 56.7	186.1	9.3	292.4	6.6	123.2	
7.....	357.907+0.107	17 40 07.36	−30 39 36.4	84.6	9.2	129.0	5.7	122.6	
8.....	358.003−0.637	17 43 18.22	−30 58 17.1	427.5	9.0	654.5	6.6	121.9	
9.....	358.118+0.006	17 41 02.35	−30 32 05.0	36.7	6.4	83.2	10.4	110.0	
10.....	358.141−1.672	17 47 46.16	−31 23 33.8	153.4	16.0	715.9	16.6	145.6	
11.....	358.154−1.680	17 47 49.85	−31 23 08.0	305.0	16.0	1463.6	17.4	145.7	
12.....	358.157+0.027	17 41 03.27	−30 29 24.2	166.4	6.0	270.8	6.7	107.4	
13.....	358.267+0.037	17 41 17.10	−30 23 30.9	89.9	5.0	124.2	5.6	100.8	
14.....	358.416−0.026	17 41 53.85	−30 17 54.9	43.3	4.0	59.8	4.7	91.4	
15.....	358.440−0.212	17 42 41.30	−30 22 35.5	55.5	4.0	92.4	7.4	90.8	
16.....	358.475−0.741	17 44 51.94	−30 37 24.8	29.8	4.7	39.0	5.0	97.6	
17.....	358.554−0.965	17 45 56.61	−30 40 23.4	44.7	5.0	55.3	3.0	100.1	PSR
18.....	358.556−0.572	17 44 23.48	−30 27 59.4	29.0	3.8	40.3	5.0	88.6	
19.....	358.586−1.528	17 48 15.95	−30 56 16.4	55.1	8.7	127.4	10.5	120.8	
20.....	358.591−1.515	17 48 13.61	−30 55 34.1	62.6	8.4	115.9	7.7	119.7	
21.....	358.592+0.044	17 42 03.10	−30 06 42.5	283.8	3.3	351.9	4.5	81.2	
22.....	358.607+1.438	17 36 39.14	−29 21 25.1	213.1	8.5	287.1	5.4	120.0	
23.....	358.615−0.036	17 42 25.35	−30 08 03.3	46.9	3.2	231.9	17.3	80.1	
24.....	358.633−0.124	17 42 48.69	−30 09 56.1	36.8	3.1	58.9	6.5	78.4	
25.....	358.634+0.060	17 42 05.41	−30 04 05.6	31.9	3.2	186.6	20.3	79.3	IRAS
26.....	358.638−1.162	17 46 55.97	−30 42 13.2	175.4	5.4	251.7	5.8	103.3	
27.....	358.645−0.035	17 42 29.53	−30 06 31.6	18.7	3.1	104.9	19.7	78.0	
28.....	358.664+0.726	17 39 33.53	−29 41 22.0	34.9	3.9	44.9	8.5	89.8	
29.....	358.684−0.118	17 42 54.85	−30 07 08.6	29.7	3.0	101.7	14.4	76.1	
30.....	358.687−1.511	17 48 26.41	−30 50 30.2	41.5	7.5	42.5	5.2	115.7	
31.....	358.697+0.260	17 41 27.62	−29 54 31.8	35.2	3.0	42.5	8.1	77.1	
32.....	358.756+0.972	17 38 49.66	−29 28 50.1	23.7	4.3	27.6	7.7	93.9	
33.....	358.786+1.265	17 37 45.84	−29 17 54.1	177.4	5.6	244.6	4.9	105.0	IRAS
34.....	358.800−0.121	17 43 12.35	−30 01 19.0	14.7	2.7	14.6	9.8	69.0	IRAS
35.....	358.804−0.012	17 42 47.43	−29 57 41.1	18.5	2.6	22.2	7.4	68.3	YSO
36.....	358.814+1.562	17 36 41.06	−29 06 56.9	46.3	8.0	103.6	7.2	118.0	
37.....	358.840−0.193	17 43 35.18	−30 01 32.6	15.2	2.6	19.0	12.2	66.8	
38.....	358.845−1.599	17 49 10.16	−30 45 07.4	227.8	7.3	317.8	5.2	114.4	
39.....	358.849+0.153	17 42 15.07	−29 50 11.2	27.4	2.6	45.2	7.1	67.1	
40.....	358.849+0.159	17 42 13.63	−29 49 56.8	98.9	2.6	153.6	5.6	66.6	
41.....	358.874+0.275	17 41 49.96	−29 45 02.1	71.1	2.6	102.1	5.7	66.8	
42.....	358.892+1.406	17 37 28.82	−29 08 01.6	107.9	6.0	144.5	4.6	107.7	X, Sy1
43.....	358.897+1.285	17 37 57.51	−29 11 39.2	34.2	5.2	63.2	7.8	101.7	
44.....	358.901+1.638	17 36 36.31	−29 00 07.8	106.8	8.3	181.6	7.1	119.0	
45.....	358.918+0.071	17 42 44.38	−29 49 15.7	95.3	2.4	1623.5	6.4	62.2	
46.....	358.922+0.138	17 42 29.21	−29 46 56.4	12.9	2.4	13.5	2.7	62.0	YSO
47.....	358.926−0.326	17 44 19.04	−30 01 20.2	13.4	2.4	34.5	10.2	63.5	
48.....	358.930+0.008	17 43 00.91	−29 50 35.4	13.3	2.4	15.4	6.8	60.9	IRAS
49.....	358.932−1.198	17 47 46.86	−30 28 15.4	129.6	4.1	221.7	7.7	92.2	
50.....	358.934−1.200	17 47 47.78	−30 28 12.2	97.7	4.1	174.7	7.5	92.2	
51.....	358.948+1.234	17 38 16.89	−29 10 43.5	67.8	4.6	99.5	6.1	97.4	
52.....	358.955−1.045	17 47 13.76	−30 22 20.6	73.2	3.5	110.4	6.3	84.5	IRAS, PN?
53.....	358.972−0.181	17 43 51.62	−29 54 24.1	16.4	2.3	43.0	10.9	59.0	
54.....	358.981+0.018	17 43 06.04	−29 47 41.5	14.1	2.3	15.7	12.7	57.8	
55.....	358.983+0.578	17 40 54.92	−29 29 50.3	142.8	2.6	164.5	3.1	68.7	
56.....	359.011−0.003	17 43 15.27	−29 46 49.9	49.6	2.2	77.1	6.2	55.8	
57.....	359.019−1.571	17 49 28.47	−30 35 18.5	68.8	5.9	100.2	6.1	107.1	
58.....	359.096−1.443	17 49 08.80	−30 27 22.4	40.8	4.7	78.1	8.9	98.1	
59.....	359.145+0.826	17 40 20.80	−29 13 43.8	20.6	2.7	29.6	5.8	71.0	
60.....	359.150−0.529	17 45 39.45	−29 56 15.1	12.2	2.2	13.7	2.9	56.0	
61.....	359.150−2.247	17 52 29.24	−30 49 16.7	89.7	14.5	318.8	14.6	140.5	
62.....	359.159−0.037	17 43 44.91	−29 40 20.1	10.7	2.0	37.2	14.4	47.3	IRAS, YSO
63.....	359.180−2.292	17 52 44.41	−30 49 03.9	183.7	15.2	334.4	7.5	142.6	PN

TABLE 2—Continued

GCPS No. (1)	Name (2)	R.A. (J2000) (3)	Decl. (J2000) (4)	I (mJy beam ⁻¹) (5)	rms (mJy beam ⁻¹) (6)	S (mJy) (7)	θ (arcsec) (8)	Offset (arcmin) (9)	SIMBAD Match ^a (10)
64.....	359.204+1.397	17 38 16.53	-28 52 30.7	31.5	4.6	54.3	7.8	97.4	
65.....	359.212+1.901	17 36 21.39	-28 35 52.7	476.0	9.8	643.3	5.2	125.0	
66.....	359.229+1.979	17 36 05.76	-28 32 30.4	274.0	11.0	706.8	9.7	129.0	
67.....	359.235+0.102	17 43 23.01	-29 32 05.3	12.2	1.9	11.3	4.5	43.8	
68.....	359.260+1.385	17 38 27.58	-28 50 02.4	23.8	4.4	36.5	5.3	95.2	
69.....	359.264-2.297	17 52 57.42	-30 44 54.5	87.2	14.6	273.4	48.2	140.7	
70.....	359.300-0.134	17 44 28.12	-29 36 10.8	34.6	1.9	83.4	9.9	39.3	
71.....	359.305-0.841	17 47 15.71	-29 58 00.0	77.2	2.4	213.3	10.4	60.7	X, PSR
72.....	359.326-0.567	17 46 13.80	-29 48 24.3	17.1	2.0	47.6	11.2	48.5	
73.....	359.348-0.239	17 44 59.77	-29 37 01.9	10.7	1.8	16.0	12.8	37.1	
74.....	359.359-0.981	17 47 56.66	-29 59 37.2	29.1	2.5	76.7	11.1	66.0	X, PN
75.....	359.387-1.764	17 51 07.09	-30 22 17.5	59.6	6.2	70.4	3.2	108.4	
76.....	359.389+0.459	17 42 21.85	-29 12 56.0	12.2	2.0	77.4	21.0	45.0	
77.....	359.391+1.272	17 39 13.05	-28 47 00.8	141.2	3.6	294.0	7.9	85.9	
78.....	359.394+1.270	17 39 13.82	-28 46 55.1	73.3	3.6	80.1	7.3	85.8	
79.....	359.413+0.007	17 44 11.20	-29 25 57.5	10.7	1.8	15.1	5.9	31.7	YSO
80.....	359.432+0.130	17 43 45.15	-29 21 09.4	15.9	2.0	82.6	10.2	44.0	
81.....	359.460-1.246	17 49 13.84	-30 02 35.1	23.9	3.1	24.0	1.6	77.5	PSR
82.....	359.465-0.169	17 45 00.07	-29 28 49.5	14.1	1.7	25.9	8.1	29.4	IRAS, YSO, X
83.....	359.467-0.174	17 45 01.49	-29 28 54.2	11.7	1.7	37.6	13.6	29.3	IRAS, YSO, X
84.....	359.473+1.247	17 39 30.74	-28 43 40.4	64.5	3.4	97.9	5.6	82.7	
85.....	359.476+1.241	17 39 32.34	-28 43 42.4	66.8	3.4	98.0	5.4	82.4	
86.....	359.483-0.218	17 45 14.28	-29 29 27.2	11.0	1.7	24.9	10.3	29.5	
87.....	359.535-1.736	17 51 21.46	-30 13 48.9	72.0	5.5	182.5	10.2	104.0	
88.....	359.545-1.147	17 49 02.46	-29 55 09.8	123.6	2.7	170.8	4.6	70.4	
89.....	359.547+0.986	17 40 41.97	-28 48 10.7	93.9	2.6	248.9	11.5	66.4	
90.....	359.558+0.801	17 41 26.51	-28 53 29.7	23.9	2.2	75.3	13.5	56.0	PN
91.....	359.568+1.145	17 40 08.21	-28 42 04.2	65.3	2.9	295.7	16.4	74.9	
92.....	359.591+1.051	17 40 33.26	-28 43 52.1	15.7	2.7	50.8	13.3	69.4	
93.....	359.605+0.305	17 43 29.20	-29 06 48.0	44.1	1.7	154.8	13.3	29.3	
94.....	359.628+1.311	17 39 38.28	-28 33 44.7	64.6	3.4	199.7	11.5	83.8	
95.....	359.646-0.057	17 44 59.75	-29 16 03.1	15.2	1.7	105.0	22.3	18.3	YSO
96.....	359.657-0.067	17 45 03.69	-29 15 48.8	14.0	1.7	82.2	18.7	17.8	YSO
97.....	359.673-1.278	17 49 51.99	-29 52 37.6	21.3	3.0	36.2	6.9	75.5	
98.....	359.710-0.586	17 47 13.23	-29 29 19.0	80.2	1.8	129.1	6.9	35.4	
99.....	359.710-0.903	17 48 28.29	-29 39 08.8	112.8	2.2	175.6	5.6	53.5	
100.....	359.712-0.907	17 48 29.52	-29 39 08.6	127.1	2.2	265.3	8.4	53.7	
101.....	359.733+1.139	17 40 33.31	-28 33 53.6	15.0	2.8	35.4	10.4	72.5	
102.....	359.733-1.854	17 52 17.45	-30 07 10.9	149.9	6.3	192.2	4.9	109.3	
103.....	359.744-0.590	17 47 19.11	-29 27 39.9	22.3	1.8	76.3	14.0	34.5	IRAS
104.....	359.745+0.818	17 41 49.73	-28 43 26.9	11.8	2.1	16.9	4.7	53.3	
105.....	359.764-1.980	17 52 52.11	-30 09 25.3	82.8	7.7	109.8	4.9	116.5	
106.....	359.770-0.459	17 46 51.97	-29 22 14.7	8.5	1.7	49.2	19.7	27.0	
107.....	359.776-0.450	17 46 50.74	-29 21 41.5	11.0	1.7	29.7	12.0	26.0	
108.....	359.778+1.985	17 37 24.74	-28 04 32.0	245.7	9.1	277.5	3.0	122.4	
109.....	359.780+0.522	17 43 03.49	-28 51 02.3	24.4	1.8	111.6	17.2	35.8	
110.....	359.832-0.877	17 48 39.55	-29 32 04.2	16.8	2.1	20.0	7.7	50.5	
111.....	359.845-1.845	17 52 31.25	-30 01 06.6	562.8	6.1	764.0	5.5	108.2	
112.....	359.868-1.509	17 51 14.39	-29 49 40.3	44.7	3.7	53.3	4.0	87.7	
113.....	359.873+0.177	17 44 37.48	-28 57 08.6	87.2	1.6	508.7	19.6	14.1	YSO
114.....	359.900-1.060	17 49 32.33	-29 34 11.7	38.0	2.4	81.6	9.5	60.9	IR
115.....	359.912-1.815	17 52 33.43	-29 56 44.7	326.9	5.8	473.8	6.2	105.9	
116.....	359.923-1.837	17 52 40.31	-29 56 52.5	129.1	6.0	186.6	6.1	107.2	
117.....	359.931-0.876	17 48 53.33	-29 26 57.1	34.9	2.1	49.9	5.7	49.5	
118.....	359.978-1.314	17 50 43.71	-29 38 00.4	30.1	3.0	40.1	2.8	75.8	
119.....	359.986+1.382	17 40 13.78	-28 13 16.4	85.0	3.6	177.8	8.5	85.7	
120.....	359.988-0.544	17 47 43.04	-29 13 42.5	10.1	1.8	14.4	8.8	29.8	
121.....	359.993+1.590	17 39 27.04	-28 06 17.0	105.8	4.7	214.1	5.9	98.2	
122.....	0.005-0.892	17 49 07.60	-29 23 38.4	299.0	2.1	568.0	8.7	50.7	
123.....	0.028+0.622	17 43 16.09	-28 35 12.6	10.6	1.9	20.7	6.0	40.3	
124.....	0.059+1.903	17 38 24.31	-27 52 55.9	45.6	7.9	68.7	15.3	117.5	
125.....	0.075-1.066	17 49 58.53	-29 25 22.6	29.0	2.4	106.2	13.8	61.6	IR
126.....	0.078-0.690	17 48 30.27	-29 13 40.0	10.2	1.9	17.8	7.0	39.3	
127.....	0.107-1.217	17 50 38.78	-29 28 23.2	29.2	2.7	51.1	7.9	70.9	

TABLE 2—*Continued*

GCPS No. (1)	Name (2)	R.A. (J2000) (3)	Decl. (J2000) (4)	I (mJy beam ⁻¹) (5)	rms (mJy beam ⁻¹) (6)	S (mJy) (7)	θ (arcsec) (8)	Offset (arcmin) (9)	SIMBAD Match ^a (10)
128.....	0.111−1.392	17 51 20.85	−29 33 32.2	48.9	3.3	64.9	5.1	81.2	
129.....	0.115+0.792	17 42 48.85	−28 25 24.1	36.0	2.1	78.4	9.3	51.4	
130.....	0.119+1.160	17 41 24.37	−28 13 33.7	26.3	2.8	33.7	4.1	73.3	
131.....	0.123+0.017	17 45 50.81	−28 49 20.1	43.2	1.6	91.7	9.4	11.2	X, MC
132.....	0.131−1.068	17 50 06.94	−29 22 32.0	55.7	2.4	129.0	8.7	62.2	
133.....	0.156−0.781	17 49 02.65	−29 12 24.7	12.6	2.0	26.5	15.9	45.8	OPC
134.....	0.191−2.221	17 54 49.58	−29 54 38.6	76.3	11.6	99.5	6.4	131.2	IRAS
135.....	0.193−0.688	17 48 46.10	−29 07 37.6	21.7	1.9	29.4	5.3	41.2	
136.....	0.197−1.218	17 50 51.72	−29 23 45.7	94.3	2.8	113.6	3.8	71.7	
137.....	0.272+1.195	17 41 38.11	−28 04 39.3	224.2	3.0	259.5	2.9	77.2	
138.....	0.281−0.485	17 48 10.66	−28 56 51.1	13.3	1.8	58.9	17.1	33.1	IRAS, H II
139.....	0.285+0.407	17 44 42.93	−28 28 50.1	10.0	1.8	12.8	12.1	34.4	
140.....	0.300+0.767	17 43 21.18	−28 16 45.9	17.7	2.2	31.5	7.7	53.6	
141.....	0.306+0.392	17 44 49.17	−28 28 13.5	40.1	1.8	50.6	4.7	33.9	
142.....	0.314+1.643	17 40 00.96	−27 48 17.7	144.1	5.4	404.5	10.2	103.7	
143.....	0.315−0.195	17 47 07.55	−28 46 04.8	15.0	1.7	28.2	8.5	23.7	X
144.....	0.329−1.668	17 52 57.07	−29 30 45.6	92.5	4.9	122.0	4.9	99.9	
145.....	0.355+0.250	17 45 29.21	−28 30 11.1	23.9	1.8	24.2	3.4	30.1	
146.....	0.359+0.897	17 42 59.48	−28 09 38.4	14.6	2.4	21.9	6.4	62.0	
147.....	0.391+0.230	17 45 39.14	−28 28 57.6	22.8	1.8	27.1	6.4	32.0	IRAS, YSO
148.....	0.405+1.060	17 42 28.43	−28 02 10.6	208.9	2.8	261.1	4.6	71.7	
149.....	0.409+0.977	17 42 48.37	−28 04 33.7	36.2	2.6	127.2	13.5	67.6	
150.....	0.413+0.523	17 44 33.95	−28 18 40.2	12.9	2.0	13.0	5.7	44.5	
151.....	0.420−0.567	17 48 49.80	−28 52 13.6	11.4	1.9	41.0	13.6	42.2	IRAS
152.....	0.426−0.060	17 46 51.74	−28 36 10.0	53.5	1.7	90.7	7.5	28.6	YSO
153.....	0.441+0.586	17 44 23.41	−28 15 12.4	60.9	2.0	117.0	7.6	48.1	
154.....	0.446+1.019	17 42 43.74	−28 01 21.8	16.1	2.7	22.5	10.5	70.6	
155.....	0.450+0.591	17 44 23.63	−28 14 38.3	55.5	2.0	94.9	8.2	49.0	
156.....	0.469−0.097	17 47 06.57	−28 35 09.9	56.3	1.8	161.8	11.8	31.3	
157.....	0.473−0.677	17 49 23.13	−28 52 53.7	11.5	2.1	76.0	20.7	49.4	
158.....	0.478−0.101	17 47 08.63	−28 34 48.6	38.3	1.8	138.8	13.2	32.4	
159.....	0.481−1.598	17 53 01.55	−29 20 45.1	32.6	4.7	58.3	8.1	98.3	
160.....	0.485−0.703	17 49 30.75	−28 53 05.7	11.1	2.1	32.5	11.9	50.9	
161.....	0.491−0.699	17 49 30.78	−28 52 42.2	12.5	2.1	24.3	8.1	51.0	
162.....	0.491−0.779	17 49 49.45	−28 55 06.9	24.3	2.2	26.3	6.4	54.7	
163.....	0.491−1.044	17 50 51.90	−29 03 17.7	55.0	2.6	72.8	5.2	68.2	
164.....	0.502−2.109	17 55 06.13	−29 35 10.6	59.2	10.7	114.1	8.9	128.2	
165.....	0.538+0.261	17 45 52.89	−28 20 26.9	17.9	1.9	30.9	7.5	40.1	
166.....	0.548−0.851	17 50 14.53	−28 54 25.9	24.8	2.3	127.5	16.7	60.3	IRAS, H II
167.....	0.554−0.839	17 50 12.61	−28 53 43.7	17.1	2.3	51.0	13.0	60.0	IRAS, H II
168.....	0.562−0.819	17 50 08.87	−28 52 42.0	101.8	2.3	119.7	3.7	59.3	
169.....	0.565−0.854	17 50 17.72	−28 53 38.7	15.0	2.4	79.7	18.8	61.1	H II
170.....	0.586−0.871	17 50 24.55	−28 53 05.1	19.5	2.4	432.7	42.3	62.6	H II
171.....	0.636+1.537	17 41 11.50	−27 35 18.3	62.5	5.4	88.7	10.3	103.6	
172.....	0.653−0.340	17 48 29.25	−28 33 15.2	17.0	2.0	50.4	12.8	45.8	
173.....	0.657+1.054	17 43 05.84	−27 49 29.2	112.3	3.1	181.4	7.1	78.7	
174.....	0.663−0.853	17 50 31.23	−28 48 34.0	90.3	2.5	110.4	4.3	64.8	
175.....	0.667−0.037	17 47 19.79	−28 23 01.4	112.6	1.9	194.6	9.5	43.0	H II, X
176.....	0.677−0.224 ^b	17 48 05.50	−28 28 24.4	54.3	2.0	255.5	17.5	45.1	XRB
177.....	0.691−0.224	17 48 07.44	−28 27 42.6	32.3	2.0	52.4	7.1	46.1	
178.....	0.722+0.405	17 45 45.51	−28 06 31.7	64.7	2.2	87.0	7.6	54.0	
179.....	0.722+1.299	17 42 18.62	−27 38 28.2	60.1	4.2	81.3	2.9	93.2	
180.....	0.736−1.465	17 53 05.77	−29 03 29.3	128.9	4.6	169.2	4.6	97.4	
181.....	0.749+1.184	17 42 48.94	−27 40 39.1	20.2	3.8	21.8	5.6	88.4	
182.....	0.801−1.385	17 52 55.92	−28 57 44.0	35.2	4.4	65.6	8.3	95.3	
183.....	0.801−1.796	17 54 33.21	−29 10 10.9	59.0	7.8	308.2	17.2	116.8	
184.....	0.809−1.571	17 53 40.90	−29 02 56.3	37.9	5.6	44.5	6.9	105.1	
185.....	0.837−0.556	17 49 45.82	−28 30 27.0	14.6	2.4	13.4	4.0	61.6	
186.....	0.838−0.560	17 49 46.84	−28 30 29.3	25.1	2.4	55.1	9.2	61.8	
187.....	0.845−0.105	17 48 01.43	−28 16 05.8	12.1	2.2	45.8	15.2	53.8	IRAS, YSO
188.....	0.847+1.171	17 43 05.81	−27 36 05.0	390.0	4.0	421.0	2.3	90.6	
189.....	0.858−0.952	17 51 21.70	−28 41 31.8	34.3	3.0	47.1	4.6	77.1	
190.....	0.868−0.286	17 48 47.06	−28 20 30.9	21.3	2.3	27.9	3.8	57.2	
191.....	0.874−0.283	17 48 47.16	−28 20 08.0	92.6	2.3	141.9	6.6	57.2	

TABLE 2—Continued

GCPS No. (1)	Name (2)	R.A. (J2000) (3)	Decl. (J2000) (4)	I (mJy beam ⁻¹) (5)	rms (mJy beam ⁻¹) (6)	S (mJy) (7)	θ (arcsec) (8)	Offset (arcmin) (9)	SIMBAD Match ^a (10)
192.....	0.880+0.489	17 45 48.31	−27 55 49.4	47.9	2.5	69.1	5.9	65.0	
193.....	0.891+0.209	17 46 54.83	−28 03 56.9	13.4	2.3	18.8	9.2	59.3	
194.....	0.891+0.736	17 44 52.60	−27 47 32.1	20.1	2.9	32.0	6.8	73.8	
195.....	0.900−0.856	17 51 04.99	−28 36 26.2	17.6	2.9	27.4	9.1	75.1	
196.....	0.900−1.404	17 53 13.98	−28 53 11.4	33.2	4.9	60.7	8.1	99.5	
197.....	0.901+0.405 ^b	17 46 10.63	−27 57 22.6	36.3	2.4	183.4	18.1	63.3	
198.....	0.931−1.136	17 52 15.19	−28 43 23.1	30.2	3.8	43.2	3.9	88.1	
199.....	0.936+1.469	17 42 09.99	−27 22 08.1	63.0	6.2	82.0	4.6	108.4	
200.....	0.954−1.619	17 54 12.38	−28 56 55.2	46.4	6.8	55.1	11.1	112.1	
201.....	0.990−0.332	17 49 14.96	−28 15 39.5	18.9	2.5	36.8	12.0	65.1	YSO
202.....	0.993−1.599	17 54 13.15	−28 54 18.8	64.5	6.8	154.1	10.7	112.3	
203.....	1.003−1.595	17 54 13.65	−28 53 40.5	82.2	6.9	171.8	8.8	112.5	
204.....	1.011+0.026	17 47 54.40	−28 03 29.9	115.7	2.5	132.8	3.4	64.2	
205.....	1.012−0.372	17 49 27.29	−28 15 45.2	24.2	2.6	46.0	8.7	67.1	
206.....	1.027+1.544	17 42 05.64	−27 15 08.9	52.2	7.4	155.8	19.0	115.2	
207.....	1.028−1.112	17 52 23.09	−28 37 38.6	563.2	4.0	892.1	6.5	91.2	
208.....	1.048+1.572	17 42 02.33	−27 13 11.0	326.6	7.9	363.7	1.8	117.3	
209.....	1.062+0.381	17 46 39.09	−27 49 53.0	110.2	2.8	125.1	3.3	72.2	IRAS
210.....	1.067−1.891	17 55 32.47	−28 59 17.7	59.9	11.1	135.4	8.9	129.5	
211.....	1.094−0.275	17 49 16.28	−28 08 33.3	15.4	2.7	15.0	1.9	70.4	
212.....	1.138+0.807	17 45 11.26	−27 32 39.1	24.6	3.8	28.6	7.1	88.2	IRAS, PN
213.....	1.173−0.384	17 49 52.58	−28 07 49.8	21.0	3.0	42.9	8.3	76.7	
214.....	1.178−0.381	17 49 52.71	−28 07 28.9	22.5	3.0	31.2	5.0	76.7	
215.....	1.189−1.319	17 53 34.04	−28 35 38.9	236.6	5.9	327.2	5.4	106.7	
216.....	1.200+0.415	17 46 50.58	−27 41 44.9	22.2	3.2	21.5	4.8	80.5	
217.....	1.301+0.130	17 48 10.98	−27 45 22.7	21.1	3.3	25.0	2.6	82.0	
218.....	1.323+0.216	17 47 53.96	−27 41 35.1	20.5	3.5	20.5	4.7	84.3	
219.....	1.386−0.291	17 50 00.65	−27 54 03.1	26.0	3.7	71.1	12.0	87.3	
220.....	1.387−0.172	17 49 33.19	−27 50 18.2	22.4	3.7	37.0	4.0	86.7	
221.....	1.409−0.385	17 50 25.81	−27 55 42.3	133.5	3.9	153.8	3.0	90.3	
222.....	1.411−0.290	17 50 04.08	−27 52 41.6	22.5	3.9	43.0	8.8	89.3	
223.....	1.415−0.295	17 50 05.68	−27 52 39.7	21.1	3.9	34.7	5.6	89.6	
224.....	1.448+1.776	17 42 12.53	−26 46 20.3	82.7	14.9	80.7	11.5	141.6	
225.....	1.459+0.235	17 48 08.72	−27 34 00.4	98.7	4.2	237.3	4.9	92.9	
226.....	1.467+0.053	17 48 52.01	−27 39 15.0	33.6	4.0	32.8	6.4	91.3	
227.....	1.468+0.229	17 48 11.12	−27 33 44.8	77.6	4.2	122.8	5.6	93.1	
228.....	1.474−0.247	17 50 02.63	−27 48 08.4	66.4	4.1	124.0	8.5	92.2	IRAS
229.....	1.480−0.825	17 52 18.34	−28 05 33.6	87.0	5.4	128.9	6.3	103.3	
230.....	1.490+0.173	17 48 27.23	−27 34 20.9	23.4	4.2	35.2	5.9	93.5	
231.....	1.499−1.245	17 53 59.55	−28 17 21.0	111.9	8.0	185.7	7.5	117.7	
232.....	1.513−1.220	17 53 55.79	−28 15 52.6	187.7	8.0	357.4	8.0	117.7	
233.....	1.540−0.963	17 52 59.06	−28 06 39.3	845.4	6.5	1099.3	4.8	110.4	PSR
234.....	1.620+0.261	17 48 24.99	−27 24 55.0	28.6	5.3	38.9	11.7	102.6	
235.....	1.761−0.377	17 51 12.92	−27 37 19.9	38.8	6.5	48.8	9.8	110.7	
236.....	1.772−1.040	17 53 49.26	−27 57 01.2	62.9	9.8	97.0	6.2	125.1	IR
237.....	1.777+0.120	17 49 19.67	−27 21 14.7	39.8	6.5	51.6	4.7	110.2	
238.....	1.796−1.025	17 53 48.86	−27 55 18.1	89.3	9.9	113.4	6.1	125.5	
239.....	1.828+1.068	17 45 47.97	−26 49 08.4	168.0	11.6	375.9	7.6	131.0	
240.....	1.894+0.479	17 48 12.93	−27 04 06.8	61.5	8.7	94.3	5.6	120.8	
241.....	2.186+0.043	17 50 34.02	−27 02 31.5	78.8	12.7	80.8	4.6	134.6	

NOTES.— I is intensity, rms is the local sensitivity, S is flux density, θ is the average deconvolved size, and the offset is the distance of the source from the phase center (17^h45^m40^s.045, −29°00′27″900; J2000). Units of right ascension are hours, minutes, and seconds, and units of declination are degrees, arcminutes, and arcseconds.

^a Within 1′: (PSR) pulsar; (IRAS) *IRAS* infrared source; (YSO) young stellar object; (X) X-ray object; (PN) planetary nebula; (PN?) possible planetary nebula; (IR) ISOGAL infrared source; (XRB) X-ray binary; (H II) H II region; (OPC) open cluster; (MC) molecular cloud; (Sy1) Seyfert 1 galaxy. Stellar matches were neglected, and radio source matches are in Table 3.

^b Transient source (see Hyman et al. 2002).

westward is defined as positive Galactic angle. A schematic of this coordinate system is shown in Figure 6. This coordinate system was chosen because any given angle $d\phi$ will have equal area, $r^2 d\phi$, where r is the radius of the imaged area. Furthermore, because the sensitivity of the VLA primary

beam falls off radially from the phase center, any given $r^2 d\phi$ also has an equal sensitivity.

We assume that any Galactic or extragalactic population would be symmetric about the Galactic plane. Furthermore, both populations are assumed to be symmetric about the

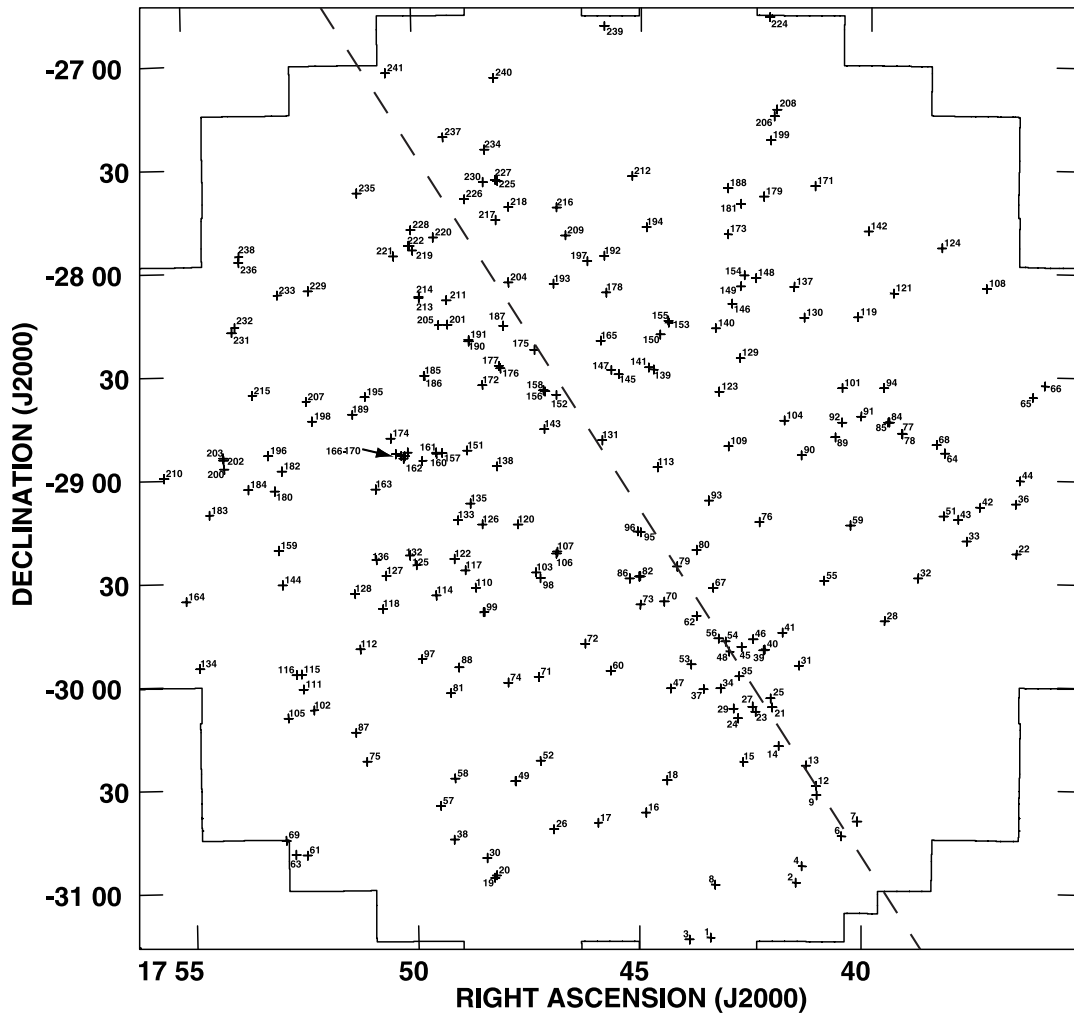


FIG. 4.—Map for locating sources in Table 2. The dashed line represents $b = 0^\circ$.

perpendicular to the Galactic plane passing through the Galactic center. The small-diameter sources were therefore reflected along these lines to place all sources in one quadrant. In this coordinate system, sources near the Galactic plane will have small Galactic angles ($\leq 35^\circ$) and sources farther from the plane will have larger Galactic angles ($\geq 55^\circ$). An unbinned Kolmogorov-Smirnov (K-S) test was performed on these data against the null hypothesis that the sources are randomly distributed. The K-S test, shown graphically in Figure 7, excludes the null hypothesis at a confidence level of 99.8% (3.6σ). Furthermore, the percentage of sources rises steeply at low Galactic angle, indicating an overdensity near the Galactic plane. The small-diameter source catalog must therefore contain a component of Galactic sources, as a purely extragalactic sample would not show clustering along the Galactic plane and indeed might be expected to show an anticorrelation due to increased scattering (Lazio & Cordes 1998a, 1998b) along the plane.

A means of understanding the nature of the small-diameter sources is via their spectral index ($S \propto \nu^\alpha$) for cases in which a higher frequency detection exists. The sources from Table 3 with 1.4 GHz GPSR (Zoonematkermani et al. 1990; Helfand et al. 1992) matches were examined, as this survey has similar sensitivity and resolution to our image. For the subset of 98 sources that matched the GPSR, we computed spectral indices and performed the K-S test to determine whether the sources

cluster along the Galactic plane. Figure 8 is a histogram of spectral indices with an overlaid Gaussian representing what would be expected from a pure extragalactic source population (De Breuck et al. 2000). Though most of the sources ($\sim 90\%$) appear to have spectral indices consistent with extragalactic sources, there is a tail of the distribution toward both flat and steep spectral indices compared with what is expected from a pure extragalactic population. Furthermore, the K-S test on sources with a GPSR match had a lower significance level (2.7σ) than the set of all sources, indicating that though some clustering along the plane may exist, the GPSR-matched set is more randomly distributed. We therefore conclude that among the sources with GPSR matches we are seeing a mostly extragalactic source population with a few ($\sim 10\%$) Galactic sources. The tail of the distribution toward steep spectral indices represents nonthermal Galactic sources (e.g., pulsars; see below), while the tail toward flat spectral indices points toward thermal sources, for example, H II regions and planetary nebulae.

Because the GPSR has such well-matched resolution and sensitivity to our image, the remaining 143 small-diameter sources ($\sim 60\%$ of our small-diameter population) are of interest because they must represent a nonthermal population of sources of relatively steep spectral index. In the area of interest, the GPSR has a detection threshold of 5–10 mJy. Figure 9 is a spectral index histogram of sources without a GPSR match

TABLE 3
RADIO CROSS-IDENTIFICATIONS

NAME	S (mJy)	ANGULAR DIAMETER (arcsec)	GPSR ^a		2LC ^b		GPSR5 ^c	
			Name	$\alpha_{0.33}^{1.4}$	Name	$\alpha_{0.33}^{1.4}$	Name	$\alpha_{0.33}^5$
357.796−0.790	234.2	10.40	357.795−0.788	−1.3
357.809−0.300	237.2	5.79	357.810−0.298	−0.7	357.808−0.299	−0.9
357.841−0.881	337.0	12.03	357.840−0.880	−1.6
357.866−0.997	881.6	15.17	357.865−0.995	−0.9
357.886+0.004	292.4	6.62	357.885+0.006	−0.9	357.885+0.005	−0.8
357.907+0.107	129.0	5.71	357.907+0.109	−1.2	357.906+0.109	−0.9
358.003−0.637	654.5	6.62	358.003−0.636	−0.4
358.118+0.006	83.2	10.38	358.116+0.007	−0.9
358.154−1.680	1463.6	17.43	358.155−1.678	−1.6
358.157+0.027	270.8	6.68	358.157+0.029	−1.0	358.157+0.029	−0.8
358.267+0.037	124.2	5.63	358.266+0.038	−1.1
358.440−0.212	92.4	7.43	358.440−0.210	−0.5	358.439−0.211	−0.3
358.475−0.741	39.0	4.99	358.476−0.739	−0.4
358.554−0.965	55.3	3.01	358.553−0.963	−0.5
358.556−0.572	40.3	5.03	358.555−0.571	−1.0
358.586−1.528	127.4	10.47	358.584−1.528	−1.0
358.591−1.515	115.9	7.65	358.590−1.513	−0.9
358.592+0.044	351.9	4.53	358.592+0.046	−1.0	358.592+0.046	−1.1
358.607+1.438	287.1	5.41	358.606+1.440	−0.8
358.634+0.060	186.6	20.31	358.633+0.063	0.3	358.633+0.062	0.1
358.638−1.162	251.7	5.77	358.638−1.160	−1.2
358.645−0.035	104.9	19.73	358.645−0.035	−0.7	358.644−0.033	−0.4
358.684−0.118	101.7	14.38	358.684−0.116	0.1
358.697+0.260	42.5	8.06	358.696+0.262	−0.3
358.786+1.265	244.6	4.94	358.786+1.268	−0.8
358.804−0.012	22.2	7.39	358.803−0.011	0.4
358.814+1.562	103.6	7.19	358.813+1.564	−1.3
358.845−1.599	317.8	5.23	358.844−1.597	−0.7
358.849+0.159	153.6	5.59	358.849+0.161	−1.0
358.874+0.275	102.1	5.71	358.873+0.277	−1.1
358.892+1.406	144.5	4.63	358.891+1.408	−0.7
358.901+1.638	181.6	7.11	358.900+1.639	−0.6
358.918+0.071	1623.5	6.43	358.918+0.073	−1.0	358.917+0.072	−0.9	358.916+0.072	−1.1
358.932−1.198	221.7	7.74	358.932−1.195	−0.9
358.934−1.200	174.7	7.47	358.934−1.198	−1.0
358.948+1.234	99.5	6.12	358.948+1.237	−0.9
358.955−1.045	110.4	6.33	358.955−1.043	−0.8
358.972−0.181	43.0	10.87	358.972−0.180	−0.4
358.983+0.578	164.5	3.07	358.983+0.580	−0.4
359.011−0.003	77.1	6.17	359.011−0.001	−0.8	359.010−0.001	−0.9
359.019−1.571	100.2	6.06	359.018−1.573	−1.8
			359.019−1.569	−1.0
359.159−0.037	37.2	14.43	359.158−0.035	−0.9
359.300−0.134	83.4	9.89	359.299−0.133	−0.7	359.300−0.133	−1.0
359.305−0.841	213.3	10.36	359.305−0.839	−0.7	359.305−0.841	1.1
			359.306−0.841	−1.3
359.359−0.981	76.7	11.09	359.358−0.980	0.9	359.357−0.980	0.9
359.389+0.459	77.4	21.01	359.388+0.460	0.1	359.388+0.460	0.1	359.388+0.460	0.2
359.391+1.272	294.0	7.88	359.391+1.274	−1.2
359.394+1.270	80.1	7.32	359.394+1.273	−0.6
359.535−1.736	182.5	10.21	359.535−1.734	−1.9
359.545−1.147	170.8	4.55	359.544−1.144	−1.1	359.544−1.146	−0.9
359.547+0.986	248.9	11.47	359.547+0.988	−0.7	359.547+0.988	−0.5
359.558+0.801	75.3	13.47	359.558+0.804	−0.6	359.558+0.803	−0.4
359.568+1.145	295.7	16.38	359.569+1.147	−0.2
359.591+1.051	50.8	13.34	359.589+1.053	−0.9
359.605+0.305	154.8	13.34	359.606+0.305	−0.7	359.604+0.307	−1.4
			359.606+0.305	−1.3	359.606+0.305	−1.1
			359.606+0.304	−0.6
359.628+1.311	199.7	11.54	359.627+1.313	−0.9
359.646−0.057	105.0	22.30	359.646−0.055	1.2
359.657−0.067	82.2	18.74	359.655−0.067	−0.5
359.673−1.278	36.2	6.92	359.674−1.276	−0.7

TABLE 3—Continued

NAME	S (mJy)	ANGULAR DIAMETER (arcsec)	GPSR ^a		2LC ^b		GPSR5 ^c	
			Name	$\alpha_{0.33}^{1.4}$	Name	$\alpha_{0.33}^{1.4}$	Name	$\alpha_{0.33}^5$
359.710−0.586	129.1	6.94	359.709−0.584	−0.6	359.708−0.585	−0.8	359.709−0.585	−0.6
			359.709−0.585	−0.9
359.710−0.903	175.6	5.57	359.709−0.902	−1.0	359.709−0.902	−0.3
359.712−0.907	265.3	8.44	359.711−0.906	−1.1
359.744−0.590	76.3	13.95	359.744−0.588	−0.3	359.744−0.588	0.1
359.776−0.450	29.7	12.01	359.775−0.449	−0.6	359.775−0.449	−0.4
			359.775−0.449	−1.7
359.780+0.522	111.6	17.19	359.781+0.523	−1.0	359.781+0.523	−0.9
359.868−1.509	53.3	3.98	359.867−1.507	−0.7
359.873+0.177	508.7	19.58	359.873+0.179	−0.4	359.872+0.178	−0.7	359.873+0.178	−1.0
			359.872+0.178	−0.7
359.900−1.060	81.6	9.53	359.903−1.057	−1.6
359.931−0.876	49.9	5.68	359.934−0.874	−0.8	359.930−0.875	−0.6
359.978−1.314	40.1	2.77	359.972−1.313	−0.5
359.986+1.382	177.8	8.54	359.972+1.384	−1.3
359.993+1.590	214.1	5.90	359.972+1.591	−1.4
			0.000+1.591	−1.1
0.005−0.892	568.0	8.67	0.000−0.889	−0.5	0.005−0.890	−1.3
0.075−1.066	106.2	13.78	0.074−1.063	−0.7
0.111−1.392	64.9	5.07	0.112−1.390	−0.7
0.115+0.792	78.4	9.33	0.114+0.793	−0.9
0.131−1.068	129.0	8.70	0.131−1.065	−1.4
			0.131−1.067	−2.0
0.193−0.688	29.4	5.34	0.191−0.686	0.4	0.192−0.687	0.5	0.192−0.687	0.2
0.197−1.218	113.6	3.80	0.198−1.216	−0.9
0.272+1.195	259.5	2.89	0.271+1.198	−1.1
0.281−0.485	58.9	17.10	0.279−0.482	0.4	0.280−0.483	0.7	0.280−0.483	0.4
0.300+0.767	31.5	7.69	0.299+0.769	−0.9
0.306+0.392	50.6	4.70	0.305+0.394	−0.6	0.306+0.394	−0.7
			0.305+0.394	−0.7
			0.305+0.394	−0.5
0.314+1.643	404.5	10.17	0.314+1.643	−1.3
0.315−0.195	28.2	8.45	0.314−0.194	0.8
0.329−1.668	122.0	4.89	0.328−1.666	−0.9
0.391+0.230	27.1	6.43	0.391+0.231	−0.7
0.405+1.060	261.1	4.58	0.405+1.062	−0.8	0.404+1.062	−0.7
0.426−0.060	90.7	7.48	0.426−0.058	−0.1	0.426−0.058	−0.2
0.441+0.586	117.0	7.55	0.441+0.588	−1.4	0.440+0.587	−0.3
0.478−0.101	138.8	13.18	0.477−0.100	−0.3	0.477−0.100	−0.4
0.481−1.598	58.3	8.08	0.481−1.595	−1.2
0.485−0.703	32.5	11.85	0.486−0.701	0.1
0.491−0.779	26.3	6.39	0.491−0.777	−0.3
0.491−1.044	72.8	5.23	0.491−1.042	−0.5	0.490−1.043	−0.8
0.548−0.851	127.5	16.70	0.548−0.849	0.7	0.546−0.852	1.0
0.538+0.261	30.9	7.50	0.539+0.263	0.3	0.538+0.262	0.7	0.537+0.263	0.5
			0.538+0.262	0.7
0.562−0.819	119.7	3.73	0.562−0.816	−0.9	0.562−0.817	−0.8
0.636+1.537	88.7	10.31	0.634+1.539	−0.7
0.657+1.054	181.4	7.05	0.656+1.056	−0.9
0.663−0.853	110.4	4.34	0.662−0.852	−0.8	0.662−0.852	−0.8
0.667−0.037	194.6	9.51	0.668−0.035	0.5	0.667−0.035	1.4	0.667−0.036	1.1
			0.667−0.035	2.3
			0.667−0.035	1.5
0.736−1.465	169.2	4.56	0.738−1.463	−0.8
0.847+1.171	421.0	2.33	0.846+1.173	−0.7
0.858−0.952	47.1	4.57	0.858−0.950	−0.4
0.874−0.283	141.9	6.60	0.873−0.282	0.5	0.872−0.282	−0.9
0.900−1.404	60.7	8.14	0.899−1.402	−0.9
0.931−1.136	43.2	3.93	0.931−1.134	−0.9
0.936+1.469	82.0	4.64	0.936+1.471	−1.5
0.954−1.619	55.1	11.13	0.954−1.617	−0.8
0.993−1.599	154.1	10.69	0.991−1.598	−2.0
1.003−1.595	171.8	8.77	1.003−1.594	−1.1
1.011+0.026	132.8	3.39	1.011+0.027	−0.7	1.010+0.028	−0.9

TABLE 3—Continued

NAME	S (mJy)	ANGULAR DIAMETER (arcsec)	GPSR ^a		2LC ^b		GPSR5 ^c	
			Name	$\alpha_{0.33}^{1.4}$	Name	$\alpha_{0.33}^{1.4}$	Name	$\alpha_{0.33}^5$
1.027+1.544	155.8	19.0	1.025+1.545	−2.0
			1.026+1.546	−1.8
1.028−1.112	892.1	6.51	1.028−1.110	−1.2
1.048+1.572	363.7	1.82	1.047+1.574	−0.6
1.062+0.381	125.1	3.31	1.061+0.382	−1.1	1.061+0.382	−1.2
1.138+0.807	28.6	7.13	1.139+0.809	0.6
1.189−1.319	327.2	5.41	1.189−1.316	−0.7
1.409−0.385	153.8	2.98	1.409−0.383	−0.6	1.408−0.383	−1.0
1.467+0.053	32.8	6.40	1.467+0.055	−0.6
1.480−0.825	128.9	6.33	1.480−0.822	−1.3
1.499−1.245	185.7	7.48	1.499−1.242	−0.8
1.513−1.220	357.4	8.02	1.513−1.218	−0.9
1.540−0.963	1099.3	4.79	1.540−0.961	−3.0
1.772−1.040	97.0	6.18	1.772−1.038	−0.8
1.796−1.025	113.4	6.07	1.796−1.023	−1.2
1.828+1.068	375.9	7.62	1.828+1.070	−1.3
1.894+0.479	94.3	5.55	1.893+0.480	−0.8

NOTE.—Spectral index is defined as $S \sim \nu^\alpha$.

^a Zoonmatkermani et al. 1990; Helfand et al. 1992.

^b Lazio & Cordes 2004.

^c Becker et al. 1994.

assuming a 1.4 GHz flux density of 10 mJy. Assuming this flux density value results in spectral indices that are upper limits, that is, all sources must have a spectral index at least this steep. Again overlaid is a Gaussian representing what is expected from a purely extragalactic population (De Breuck et al. 2000). While roughly 50% of the sources in the region have spectral index upper limits consistent with an extragalactic population and could be background radio galaxies falling below the sensitivity limit of the GPSR, a large number of the sources are far too steep to be consistent with being background radio galaxies. Moreover, the K-S test ruled out a null hypothesis with 5.8 σ confidence, indicating that these sources tend to strongly cluster along the Galactic plane. Hence we believe that we are detecting a population of steep spectral index sources of Galactic origin. Hypotheses for the identity of these sources are pulsars (§ 5.2.1), stellar clusters or young stellar objects (§ 5.2.2), and young Galactic SNRs (§ 5.2.3).

5.2.1. Pulsars and Pulsar Candidates

Current periodicity searches for pulsars are well known to be biased against short-period, distant, highly dispersed or scattered, and tight binary pulsars (as the recent Lyne et al. 2004 detection of J0737−3039 illustrates) (see, e.g., Cordes & Lazio 1997). As pulsars are expected to have a small diameter and a steep spectral index, this high-resolution, low-frequency survey might be expected to be a more effective tool for finding GC pulsars. For this reason, we have examined our catalog for possible pulsar candidates.

Table 4 lists four previously known pulsars that were detected by checking our small-diameter sources against the ATNF pulsar database (Manchester et al. 2004).⁵ Table 5 lists 10 known pulsars in the search area that were not detected. Low flux density at higher frequencies and high image rms due to positions far from the phase center are consistent with these nondetections, with the exception of B1737−30. In the

case of this source, higher frequency detections ($\nu > 1$ GHz; Lorimer et al. 1995; Taylor et al. 1993) indicate that the source could be marginally detected in our image. However this pulsar appears to have a spectral index turnover at frequencies below ~ 600 MHz (D. Lorimer 2004, private communication), which would explain this nondetection. Other previously known sources at comparable distances from the phase center whose higher frequency flux densities suggested they appear at 330 MHz were detected at expected levels. Hence the

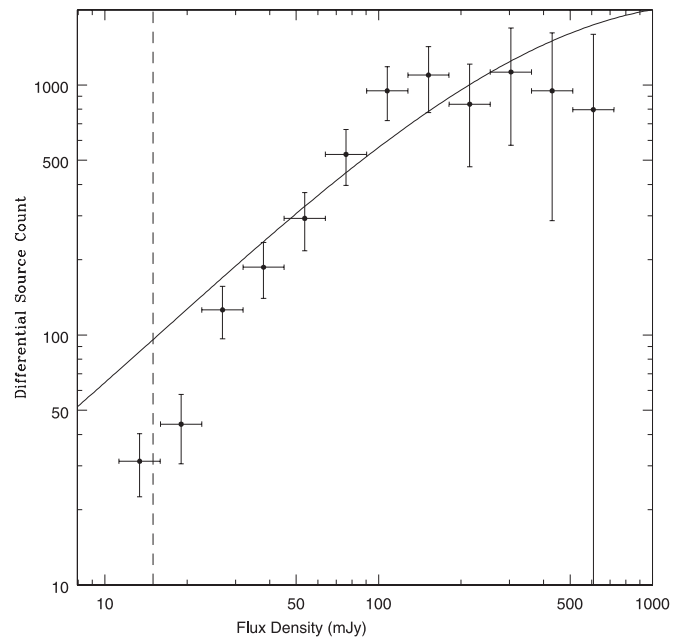


FIG. 5.—Euclidean normalized differential small-diameter source counts for the inner $1^{\circ}3$ of the Galactic center image. On the ordinate axis is plotted $S^{5/2} dN/dS$ in units of $\text{Jy}^{3/2} \text{sr}^{-1}$. The dashed line denotes the theoretical completeness limit, and the solid line shows the source counts from a deep WSRT survey (Wieringa 1991). Note the increasing difference between the WSRT observed source counts and the GC source counts with decreasing flux density.

⁵ See <http://www.atnf.csiro.au/research/pulsar/psrcat/>.

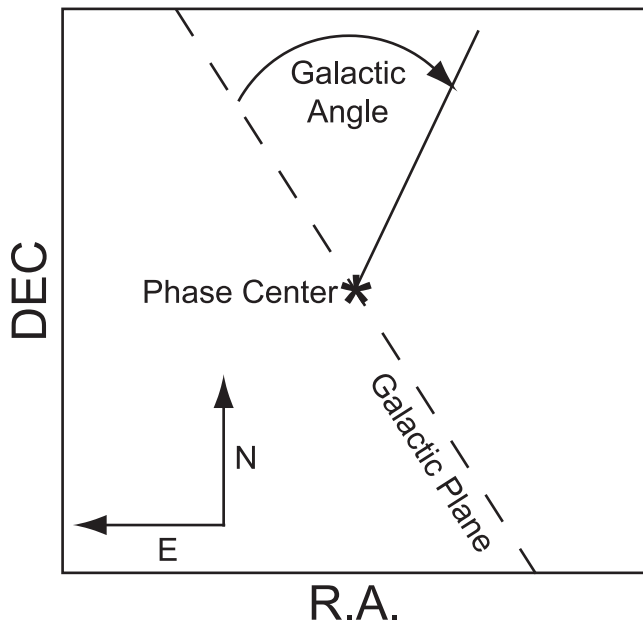


FIG. 6.—Schematic of the Galactic angle coordinate system discussed in § 5.2.

nondetection of B1737–30 is most likely not a sensitivity-related issue.

We identify 30 sources as pulsar candidates based on the following criteria: candidates must have a small diameter (deconvolved size of less than $15''$ along the major axis) and either have a steep spectrum ($\alpha_{0.33}^{1.4} \leq -1.0$) or not be detected in the 1.4 GHz GPSR (Zoonematkermani et al. 1990; Helfand et al. 1992), implying a steep spectrum. The compactness

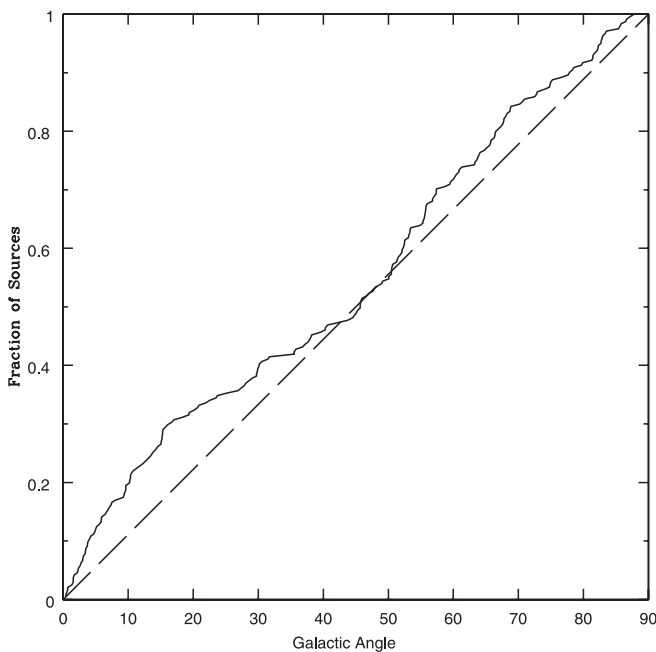


FIG. 7.—Graphical representation of the unbinned Kolmogorov-Smirnov test. The solid line is the observed distribution of Galactic angle for all sources in Table 2, and the dashed line shows the expected distribution under the null hypothesis that the sources are distributed randomly. The observed distribution rises steeply at low Galactic angles, demonstrating that the small-diameter sources tend to cluster near the plane.

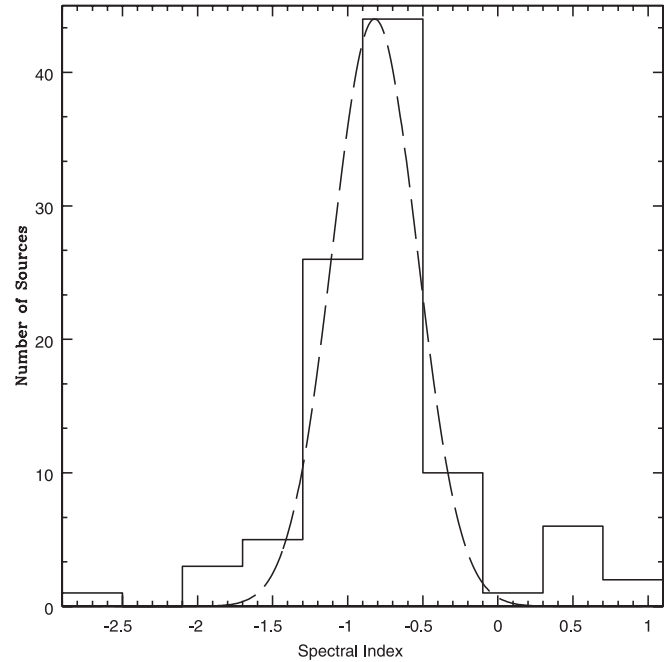


FIG. 8.—Histogram of the $\alpha_{0.33}^{1.4}$ spectral index ($S \sim \nu^\alpha$) of the 98 sources detected at 330 MHz and in the GPSR 20 cm survey (Zoonematkermani et al. 1990; Helfand et al. 1992). The Gaussian represents the distribution expected if the sources were purely extragalactic (De Breuck et al. 2000).

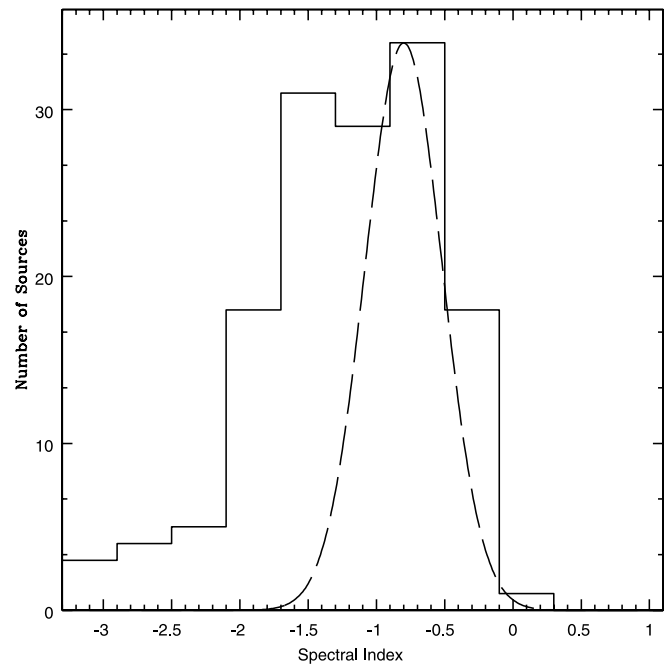


FIG. 9.—Histogram of the $\alpha_{0.33}^{1.4}$ spectral index ($S \sim \nu^\alpha$) of the 143 sources not detected in the GPSR 1.4 GHz survey (Zoonematkermani et al. 1990; Helfand et al. 1992), assuming all sources have a 1.4 GHz flux density of 10 mJy. The detection threshold of the GPSR in the area of interest is 5–10 mJy depending upon position. Note that since the 20 cm flux density is an upper limit, the spectral indices are upper limits, i.e., they may all be steeper than displayed here. The Gaussian represents the distribution expected if the sources were purely extragalactic (De Breuck et al. 2000).

TABLE 4
DETECTED PULSARS

Name	Pulsar Name	Angular Diameter (arcsec)	Flux Density (mJy)	$\alpha_{0.33}^{1.4}$
358.554–0.965	B1742–30	3.0	55.3	–0.5
359.305–0.841	J1747–2958	9.9	83.4	–0.7
359.460–1.246	B1746–30	1.6	24.0	–1.1
1.540–0.963	B1749–28	4.8	1099.3	–3.0

NOTE.—From Taylor et al. (1993) and the ATNF Pulsar Catalogue.

criterion is motivated by the observed diameter of Sgr A* at this frequency ($\sim 13''$; Nord et al. 2004) and is set at a size greater than the beam size because of the scattering discussed in the previous section. Table 6 gives the details of the pulsar candidates.

Since we have no frequency-time information on any of these sources, we cannot say how many, if any, are pulsars. However, sources on this list that are not pulsars are still interesting sources and require follow-up observations.

5.2.2. Steep-Spectrum Stellar Clusters and Young Stellar Objects

In a previous paper based partly on this image (Yusef-Zadeh et al. 2003), the low-frequency emission of the Arches stellar cluster (G0.121+0.017, GCPS G0.123+0.017 in this survey) was examined. This stellar cluster is a compact, thermal source at frequencies between 1.4 and 8 GHz but is strongly nonthermal between 0.33 and 1.4 GHz ($\alpha_{0.33}^{1.4} = -1.2 \pm 0.4$). The mechanism for this nonthermal emission is hypothesized to be colliding wind shocks, where the stellar winds of mass-losing stars collide with the ambient medium. Of the other two known young stellar clusters in the Galactic center region, the Quintuplet is undetected and the central cluster is undetectable because of its proximity to the Sgr A supernova remnant. We note that the SIMBAD matches in Table 2 have 13 sources within $1'$ of young stellar objects. It is possible that part of the population of steep-spectrum Galactic sources discussed earlier in § 5.2 is composed of such objects.

5.2.3. Young Galactic Supernova Remnants

Though six Galactic supernovae have been detected in the last 1000 years (Clark & Stephenson 1977), between 20 and 40 are thought to have occurred ($1 \text{ per } 40 \pm 10 \text{ yr}$; Tamman

TABLE 6
PULSAR CANDIDATES

Name	Angular Diameter (arcsec)	Flux Density (mJy)	$\alpha_{0.33}^{1.4}$
357.907+0.107	5.71	129	–1.2
358.157+0.027	6.68	270.8	–1.0
358.556–0.572	5.03	40.3	–1.0
358.592+0.044	4.53	351.9	–1.0
358.638–1.162	5.77	251.7	–1.2
358.687–1.511	5.2	42.5	–1.5 ^a
358.756+0.972	7.7	27.6	–1.2 ^a
358.874+0.275	5.7	102.1	–1.9 ^b
358.918+0.071	6.43	1623.5	–1.0
359.096–1.443	8.9	78.1	–1.0 ^b
359.145+0.826	5.8	29.6	–1.4 ^b
359.260+1.385	5.3	36.5	–1.4 ^b
359.387–1.764	3.2	70.4	–1.2 ^b
359.545–1.147	4.55	170.8	–1.1
359.712–0.907	8.44	265.3	–1.1
359.986+1.382	8.54	177.8	–1.3
0.107–1.217	7.9	51.1	–1.6 ^a
0.272+1.195	2.89	259.5	–1.1
0.359+0.897	6.4	21.9	–1.0 ^a
0.426–0.060	7.5	90.7	–1.0 ^a
0.481–1.598	8.08	58.3	–1.2
0.749+1.184	5.6	21.8	–1.0 ^a
0.809–1.571	6.9	44.5	–1.6 ^b
0.936+1.469	4.64	82	–1.5
1.011+0.026	3.4	132.8	–1.3 ^a
1.028–1.112	6.51	892.1	–1.2
1.062+0.381	3.31	125.1	–1.1
1.474–0.247	8.5	124.0	–1.3 ^a
1.480–0.825	6.33	128.9	–1.3
1.796–1.025	6.07	113.4	–1.2

^a Spectral index implied by nondetection in the GPSR (Zoonematkermani et al. 1990; Helfand et al. 1992) and should be considered an upper limit.

^b Spectral index measured against the NVSS (Condon et al. 1998), not the GPSR. The NVSS has a resolution of $45''$, so spectral index values should be considered an upper limit.

et al. 1994). The question of the missing SNRs was statistically addressed by Green (1991) by noting two main detection biases: SNRs must have enough surface brightness to be detected, but they also must have an angular extent more than several times the beam size in order to be identified. This

TABLE 5
PULSAR NONDETECTIONS

Pulsar Name	Distance from Phase Center (arcmin)	Flux Density (mJy ($\nu = 1.4 \text{ GHz}$))	3σ Flux Density ^a (mJy ($\nu = 0.33 \text{ GHz}$))	$\alpha_{0.33}^{1.4 \text{ b}}$ (mJy beam ^{–1})
J1738–2955	105	0.29	17.7	–2.8
B1736–29	80	2	9.9	–1.1
J1739–3023	114	1.0	21.3	–2.1
B1737–30	100	6.0	14.4	–0.6
J1740–3052	128	0.7	32.1	–2.5
J1741–2733	106	1.1	17.7	–1.9
J1741–2945	73	0.6	9.6	–1.9
J1741–3016	96	2.3	14.4	–1.3
J1747–2802	62	0.5	8.1	–1.9
J1752–2821	97	0.32	14.7	–2.7

^a The 330 MHz flux density required for a 3σ detection at location of the pulsar.

^b Lower limit based on 3σ nondetection.

results in a bias toward detection of extended, presumably older SNRs. As SNRs are nonthermal in nature and cluster strongly along the Galactic plane, a low-frequency survey for small-diameter radio sources in the Galactic center such as this one could be ideal for identifying a missing young remnant population.

Assuming an expansion rate of 2000 km s^{-1} , a 1000 yr old remnant would have a diameter of 2 pc, or $\sim 45''$ at an assumed Galactocentric distance of 8 kpc. Indeed, one such compact remnant, G1.18+0.33 with a diameter of $\sim 1'$, is detected in this image and is discussed in § 6.2. A remnant only 300 yr old or 24 kpc in distance could easily be classified as a small-diameter source ($\lesssim 25''$) in this survey (Table 2).

Actual identification of young SNRs from our small-diameter source list is difficult. SNRs typically have a spectral index of $-0.7 < \alpha < 0.0$, making identification by spectral index difficult in a field dominated by background radio galaxies of nearly the same spectral index range. SNRs can be significantly polarized, but depolarization by the intervening interstellar medium makes polarization work at 330 MHz difficult. The only possible identifier is morphology. The small-diameter sources were scrutinized by eye for evidence of shell structure, but no objects were identified in this manner. Even this identifier may be biased against identifying plerion-type SNRs. Thus while some of these sources may be young Galactic SNRs, we have no way of identifying them from among our detected small-diameter sources.

5.3. Evidence for a Scattering Screen

Interstellar free electron scattering toward the Galactic center is known to be both large (van Langevelde et al. 1992; Frail et al. 1994; Lazio & Cordes 1998a, 1998b; Bower et al. 1999) and potentially spatially variable (Lazio et al. 1999). The recent NE2001 model (Cordes & Lazio 2003) describes the scattering toward the Galactic center by a smoothly distributed screen, as well as areas of strong scattering needed to predict large or anomalous scattering toward certain sources. The expected amplitude of angular broadening for a Galactic source seen through this screen is approximately $12''$, based on the diameters of Sgr A* and various OH masers when scaled to 330 MHz. Sources closer than the Galactic center will have smaller scattering diameters, while more distant objects will be more heavily broadened, potentially by a large amount. The angular broadening of an extragalactic source may range from small (less than our beam diameter) to extremely large (many arcminutes), depending upon the porosity of the scattering screen.

Our survey is at a single frequency, so we cannot attribute the diameter of our sources exclusively to interstellar scattering, as intrinsic source structure may also contribute. Nonetheless, the spatial density of sources in our survey, combined with its relatively low observation frequency, means that scattering effects might still be identified in a statistical sense. Figure 10 shows the small-diameter sources in Galactic coordinates with their relative deconvolved sizes. We have checked for a correlation between source diameter and source position—both as a function of distance from the Galactic plane and as a function of distance from the phase center. We detect no correlation.

However, we do think that we are detecting the signature of the hypothesized scattering screen in differential source counts. Figure 5 clearly shows source counts fall off strongly toward lower flux density. Angular broadening conserves flux density, but sources are detected via their maximum intensity,

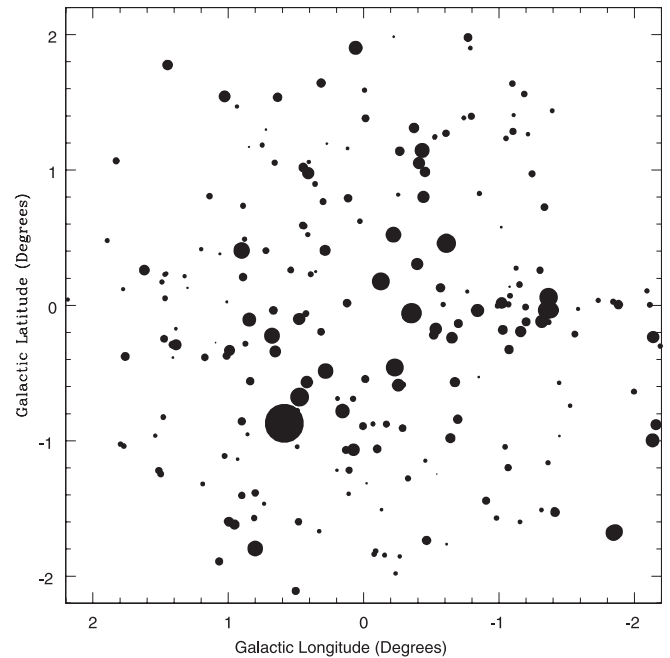


FIG. 10.—Positions and relative deconvolved sizes of all small-diameter sources in Galactic coordinates. No correlation between distance from the Galactic plane and the deconvolved source size was detected.

which will decrease as the square of the diameter of the source. For instance, a source with an intrinsic diameter of $10''$ will have its maximum intensity decreased by $\sim 45\%$ if broadened by $2''$. A source that would have been just at the detection limit would become undetectable. A source with higher intrinsic intensity would still be detectable, and its flux density would remain unchanged.

5.4. Steep Spectral Index Sources

Sensitive low-frequency observations are ideal for finding steep-spectrum sources. Several sources in our survey with cross-identifications in Table 3 have measured spectral indices that are very steep ($\alpha_{0.33}^{1.4} \leq -1.8$) and therefore require scrutiny. These sources are discussed below.

GCPS G359.535–1.736: This source has a spectral index of $\alpha_{0.33}^{1.4} = -1.9$, a deconvolved size of $10''.6 \times 3''.0$, and a position angle of 102° . A large length-to-width ratio and a position angle significantly different from that of the clean beam suggest that this source may be an unresolved radio galaxy with only a single component in the 1.4 GHz survey, akin to GCPS 0.131–1.068.

GCPS G0.131–1.068: This source is identified with two sources at 1.4 GHz (GPSR G0.131–1.065 and GPSR G0.131–10.67), with spectral indices $\alpha_{0.33}^{1.4}$ of -1.4 and -2.0 , respectively. The 330 MHz source is quite elongated, with a deconvolved size of $11''.8 \times 3''.5$, and has a position angle of 60° , significantly different from the position angle of the beam. If the flux densities of the two 1.4 GHz sources are added, the resulting spectral index is -1.1 . This source is almost certainly a blending of the two lobes of a radio galaxy.

GCPS G0.993–1.599: This source has a spectral index of $\alpha_{0.33}^{1.4} = -2.0$, has a size of $22'' \times 10''$ with a position angle of 4° , and appears slightly diffuse. If this source were associated with GPSR G1.003–1.594 ($30''$ to the north), the two sources would have the morphology of an FR II radio galaxy. A potential difficulty with this classification is the steep and quite

TABLE 7
PREVIOUSLY DETECTED NONTHERMAL FILAMENTS

Name	Maximum Intensity (mJy beam ⁻¹)	Flux Density (mJy)	Size (arcmin)	Plane Angle ^a (deg)
G0.08+0.15.....	77.7	4990	21.1 × 0.3	0, 10 ^b
G359.79+0.17.....	48.0	2540	8.3 × 0.5	35
G359.54+0.18.....	37.6	1420	6.5 × 0.8	25
G359.96+0.09.....	25.7	1450	12.5 × 0.4	15
Radio Arc.....	52.0	24000	32.0 × 4.0	5
Sgr C.....	99.7	4680	11.5 × 0.2	15
G358.85+0.47.....	7.7	106	3.2 × 0.8	90
G359.10-0.2.....	22.4	1540	22.7 × 0.4	0, 10 ^b
G359.85+0.39.....

^a Angle of the NTF with respect to the normal to the Galactic plane.

^b This NTF shows significant “kinks” and has therefore been fitted with two orientations.

different spectral indices ($\alpha_{0.33}^{1.4} = -2.0$ for GPSR G0.993–1.599 vs. $\alpha_{0.33}^{1.4} = -1.0$ for GPSR G1.003–1.594).

GCPS G1.027+1.544: This source has a size of $26'' \times 12''$ with a position angle of 148° and appears diffuse. It is identified with two sources at 1.4 GHz (GPSR G1.025–1.545 and GPSR G1.026–1.546). If the flux densities of both 1.4 GHz sources are used in determining the spectral index, the result is $\alpha_{0.33}^{1.4} = -1.4$. While morphologically this source appears to be extragalactic, its spectral index remains steeper than is common for extragalactic sources.

GCPS G1.540–0.961: This source is a known pulsar, PSR B1749–27. We derive an $\alpha_{0.33}^{1.4}$ spectral index of -3.0 for this source.

5.5. Sagittarius A*

Sagittarius A*, the radio source associated with our Galaxy’s central massive black hole, was detected utilizing a subset of these data. This is the first detection of this source at comparable frequencies, and the lowest-frequency detection to date. This detection, as well as implications for emission mechanisms and the location of Sgr A* with respect to other objects in the Sgr A region, is detailed in Nord et al. (2004).

6. EXTENDED SOURCES

Given the relatively high resolution of this image, a short discussion on why new extended sources were discovered is warranted. At a resolution of $45''$ as in LaRosa et al. (2000), large areas of the GC region are dominated by diffuse flux density, which is resolved out in this image. This allows for these regions to be searched for features that are unresolved or only moderately resolved in one dimension, that is, NTFs. Secondly, several sources appear unresolved to LaRosa et al. but are now resolved at this higher resolution.

Among the most fascinating of the unique structures in the Galactic center are the NTFs. These are remarkably coherent magnetic structures that extend tens of parsecs and maintain widths of only a few tenths of a parsec (see, e.g., Lang et al. 1999). It has been hypothesized that the NTFs are part of a globally ordered space-filling magnetic field (e.g., Morris & Serabyn 1996), and if so they would be the primary diagnostic of the GC magnetic field. An alternative idea is that the NTFs are magnetic wakes formed from the amplification of a weak global field through a molecular cloud–Galactic center wind interaction (Shore & LaRosa 1999)

TABLE 8
NEW NONTHERMAL FILAMENTS AND CANDIDATES

Name	Maximum Intensity (mJy beam ⁻¹)	Flux Density (mJy)	Size (arcmin)	Plane Angle ^a (deg)
G359.12+0.66.....	11.9	647	15.6 × 0.2	35
G359.22-0.16 ^b	23.4	269	1.8 × 0.5	55
G359.33-0.42.....	13.9	81.0	2.4 × 0.2	55
G359.36+0.09.....	10.7	65.2	2.5 × 0.2	60
G359.40-0.03.....	11.9	93.8	1.8 × 0.2	5
G359.40-0.07.....	40.6	229	1.7 × 0.3	40
G359.43+0.13.....	18.8	265	2.4 × 0.3	0, 90 ^c
G359.59-0.34.....	20.8	188	2.3 × 0.2	25
G359.66-0.11.....	9.9	226	3.5 × 0.5	20
G359.85-0.02.....	8.5	173	1.8 × 0.2	90
G359.86-0.24.....	11.2	205	8.1 × 0.2	35
G359.88-0.07.....	33.8	930	1.6 × 0.2	5
G359.90+0.19.....	11.9	129	2.4 × 0.2	35
G359.99-0.54.....	9.4	88.8	8.6 × 0.2	30
G0.02+0.04.....	22.3	228	2.0 × 0.3	0
G0.06-0.07.....	10.5	163	2.1 × 0.2	15
G0.37-0.07.....	14.1	128	1.1 × 0.3	5
G0.39+0.05.....	17.8	232	4.1 × 0.3	5
G0.39-0.12 ^b	16.1	731.2	10.1 × 0.3	5
G0.43+0.01.....	11.6	43.9	1.6 × 0.3	5

^a Angle of the NTF with respect to the normal to the Galactic plane.

^b Source observed to have significant 6 cm polarization (LaRosa et al. 2004).

^c May be two interacting NTFs with orientations of 0° and 90° to the Galactic plane.

Though as of yet there is no consensus as to the origin of these structures, they are known to be nonthermal in nature, and therefore high-resolution studies at low radio frequencies are important to understanding this phenomenon and for increasing the census of known NTFs.

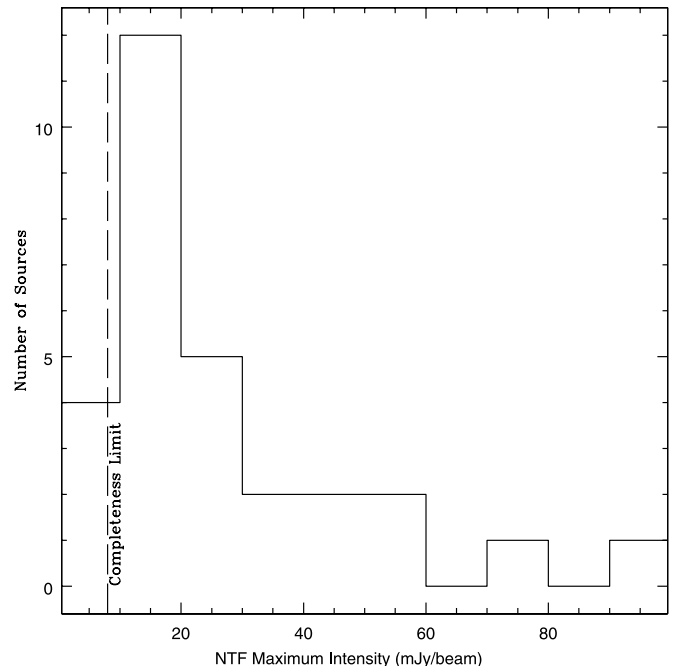


FIG. 11.—Histogram of maximum intensity for all known NTFs and NTF candidates. The dashed line represents our estimate of the minimum intensity at which we can detect NTF candidates reliably.

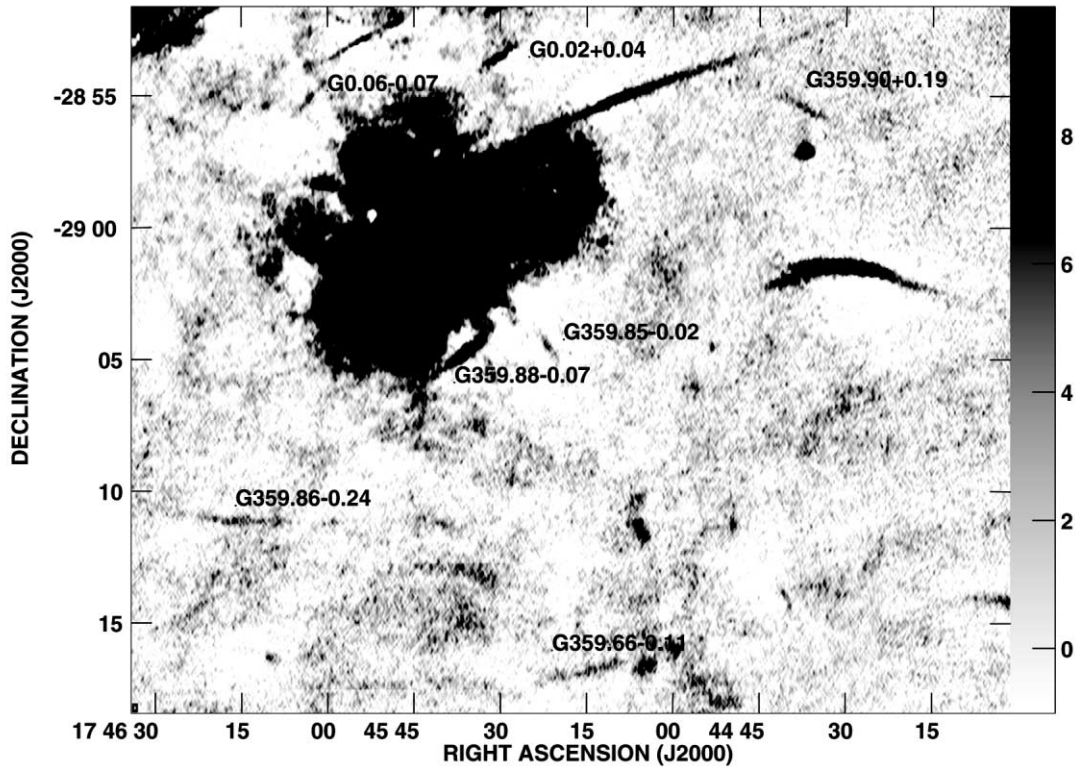


FIG. 12.—Candidate nonthermal filaments in the Sgr A region. The gray scale is linear between -1 and 10 mJy beam^{-1} . Primary-beam correction has not been applied but is negligible in this field.

Nine isolated NTFs were known before this work was completed. Of those nine, we detect eight, as we do not have sufficient surface brightness sensitivity to detect G359.85+0.39 (LaRosa et al. 2001). Table 7 summarizes the properties of the previously detected NTFs. With respect to lower resolution measurements, the filaments tend to have lower flux density

and are longer. Insensitivity to low spatial frequencies is responsible for reducing the overall flux density of the NTFs, but it also allows for extracting the fainter ends of the NTFs from the extended flux density near the Galactic center. For this reason, the flux density measurements of Table 7 should be taken only as lower limits.

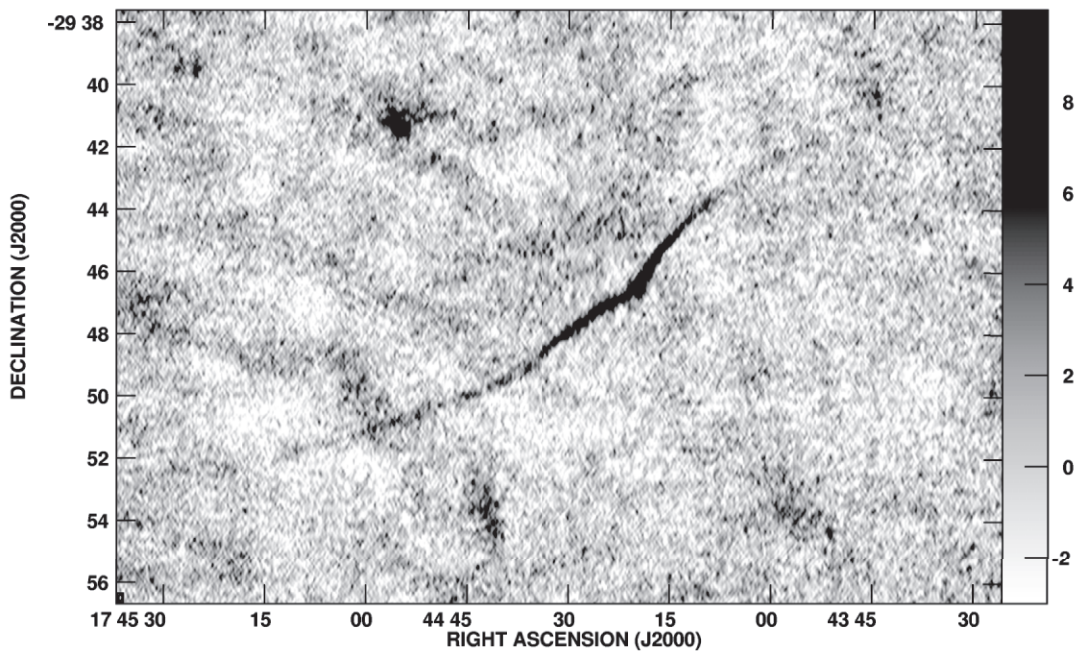


FIG. 13.—NTF G359.10-0.2 (the Snake). The gray scale is linear between -1 and 10 mJy beam^{-1} . Primary-beam correction has not been applied; the value at the center of the field is 1.29 .

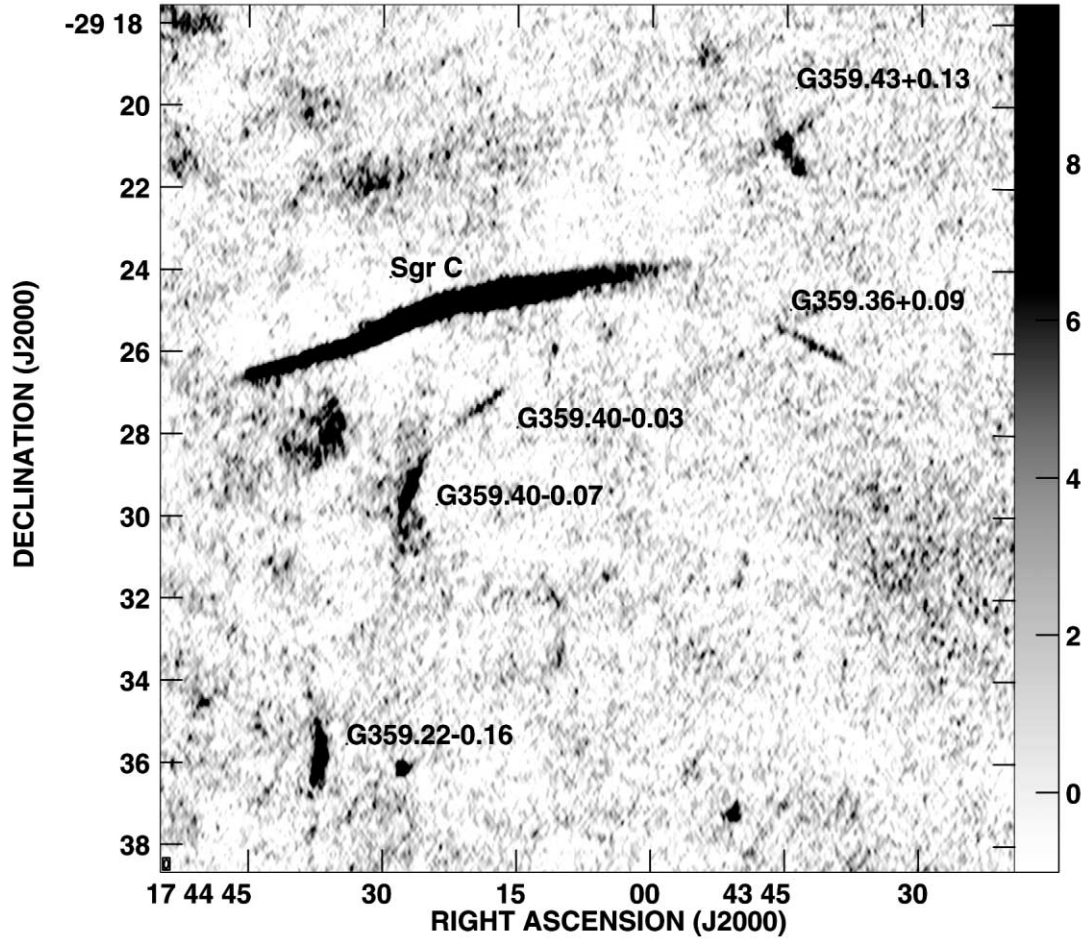


FIG. 14.—NTFs and candidates in the Sgr C region. The gray scale is linear between -1 and 10 mJy beam^{-1} . Primary-beam correction has not been applied; the value at the center of the field is 1.13 .

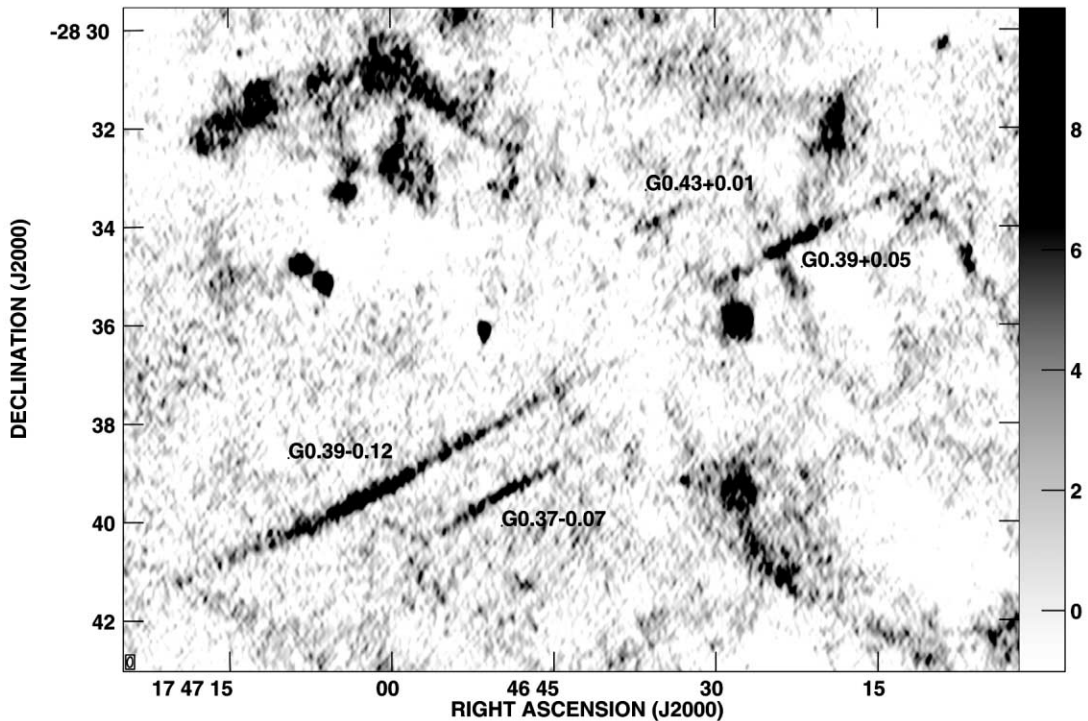


FIG. 15.—NTFs and candidates in the region between Sgr B1 and the Radio Arc, showing three candidate NTFs and one confirmed NTF similar in appearance to the filaments comprising the Galactic center Radio Arc, which is located approximately $10'$ to the south. The gray scale is linear between -1 and 10 mJy beam^{-1} . Primary-beam correction has not been applied; the value at the center of the field is 1.08 .

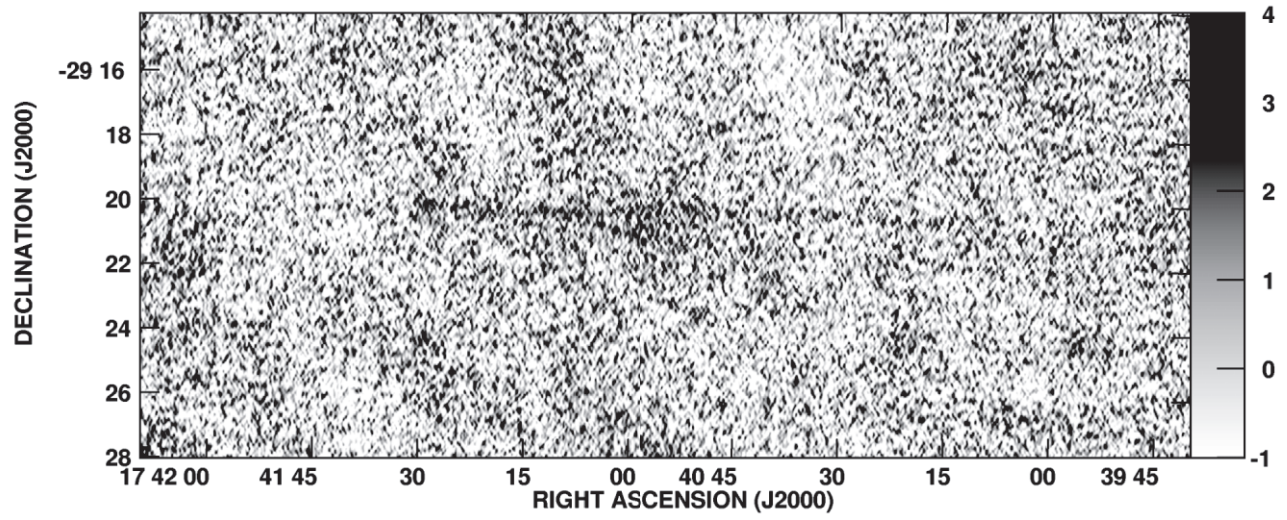


FIG. 16.—NTF candidate G359.12+0.66. The gray scale is linear between -1 and 4 mJy beam^{-1} . This source has an extremely low surface brightness and is best viewed from a distance. Primary-beam correction has not been applied; the value at the center of the field is 1.61 .

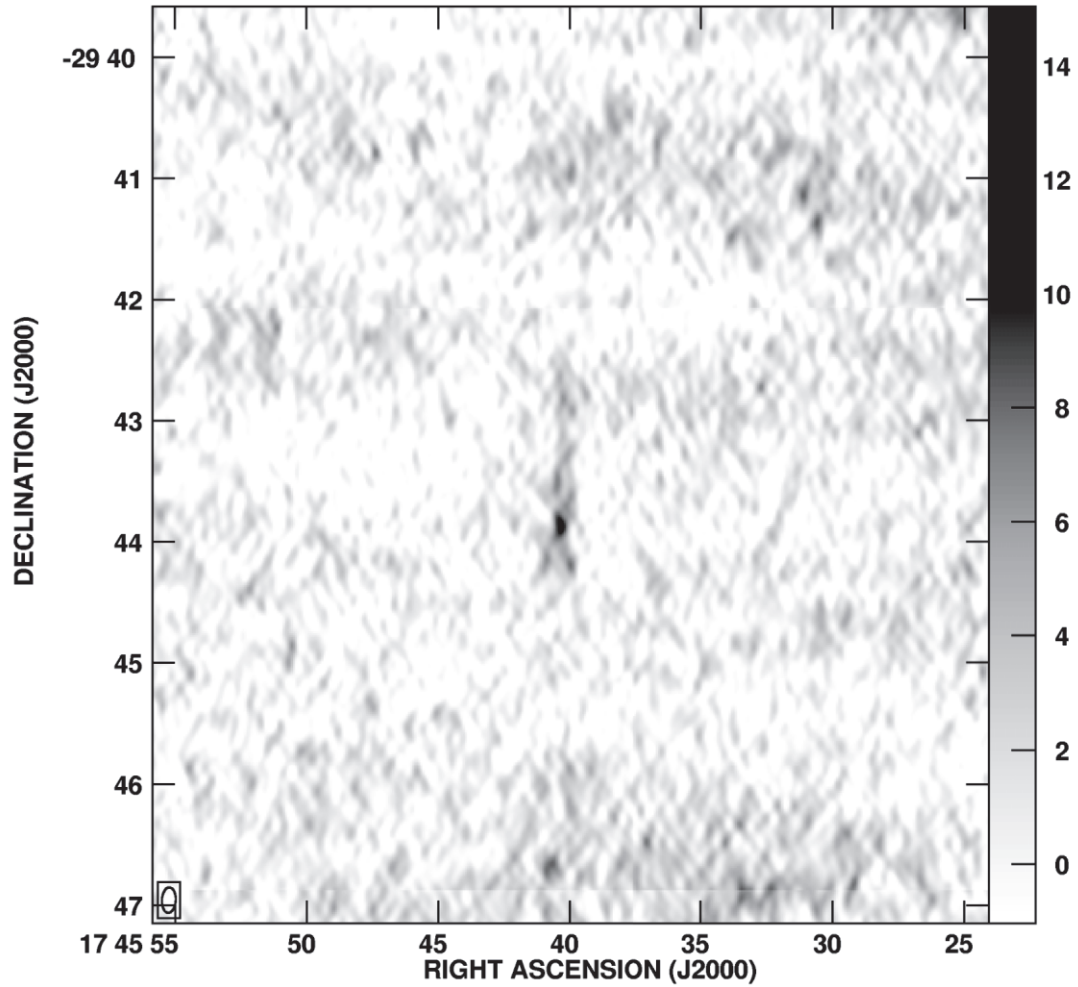


FIG. 17.—NTF candidate G359.33-0.42. The gray scale is linear between -1 and 15 mJy beam^{-1} . Primary-beam correction has not been applied; the value at the center of the field is 1.21 .

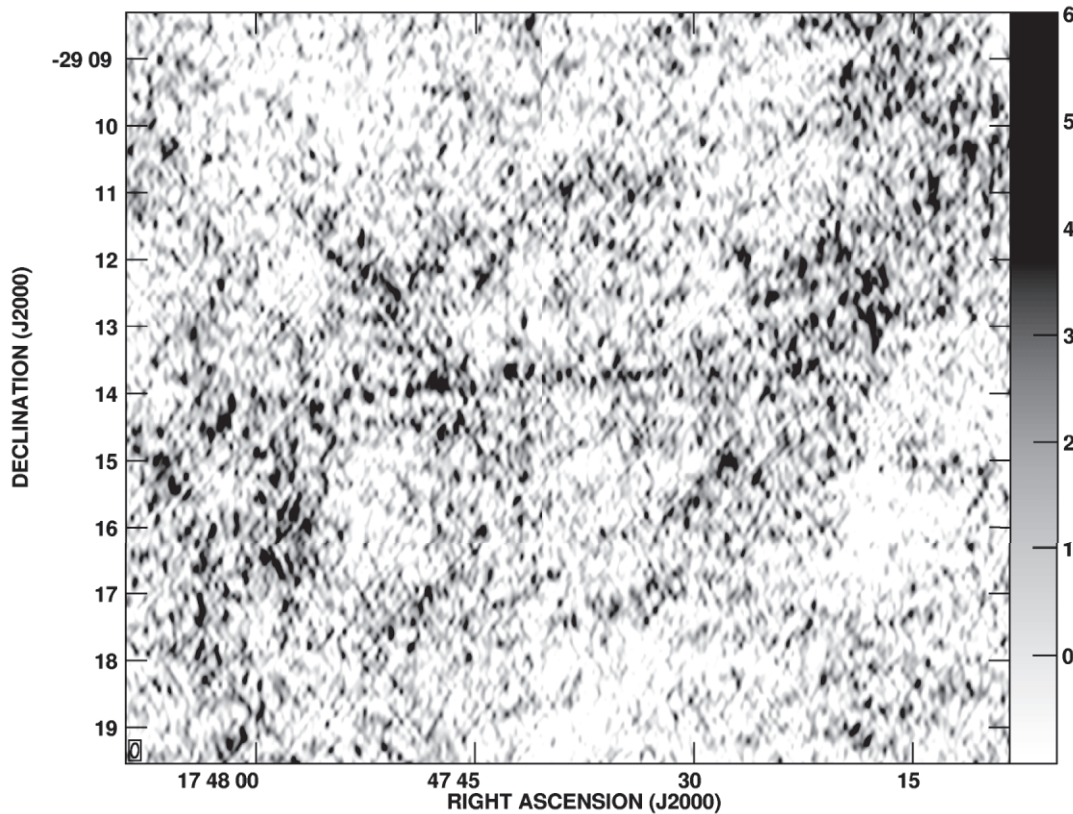


FIG. 18.—NTF candidate G359.99–0.54. The gray scale is linear between -1 and 6 mJy beam^{-1} . This source has an extremely low surface brightness and is best viewed from a distance. Primary-beam correction has not been applied; the value at the center of the field is 1.09 .

We report the detection of 20 linear structures, two of which have been confirmed as NTFs (LaRosa et al. 2004). We regard secure identifications of NTFs as those sources with large length-to-width ratios that have highly polarized ($\gtrsim 10\%$ linear polarization), nonthermal emission. With these observations, we can determine only morphology and spectrum where higher frequency observations are available. Without polarization information, we shall classify the remaining 18 objects as NTF candidates. Table 8 summarizes the properties of these 20 linear structures.

If all these NTF candidates are eventually confirmed as NTFs, the total number of known NTFs would triple. Figure 11 shows the intensity histogram of NTFs and NTF candidates. We show the intensity rather than flux density for two reasons. First, detections of these sources are based on maximum intensity, not flux density. Secondly, baseline subtraction can be difficult for extended sources that pass through regions of diffuse flux density, so the total flux density of the NTFs is uncertain. Clearly apparent in Figure 11 is a rapid increase in the number of potential NTFs at low intensity. The range of intensities is fairly small, but the increase in number rises faster than linearly with decreasing intensity. By increasing sensitivity by a factor of ~ 5 over LaRosa et al. (2000), we have tripled the number of known and suspected NTFs, suggesting that the number of NTFs rises at minimum as $N \sim I^{-0.7}$. We conclude that just the tip of the NTF luminosity distribution is being detected, and we hypothesize that there may be hundreds of low surface brightness NTFs in the GC region.

LaRosa et al. (2004) discuss the properties of the emerging NTF population in detail, but here we briefly review several noteworthy properties. First, the new NTFs significantly increase the volume of space over which the NTF phenomenon

is known to occur. Though G359.10–0.2 remains the farthest southern extent of the NTF phenomenon, new candidate NTFs are now found north, east, and west of those previously known. The entire population of suspected NTFs now covers ~ 2 square degrees, over Galactic longitudes from $+0.4$ to -0.9 and Galactic latitudes from $+0.7$ to -0.5 . This observation is of particular importance to NTF models that assume a space-filling poloidal field, as the volume over which this field must exist and, therefore, the magnetic energy in the field are now significantly increased. Of further note is the space distribution of the new candidate NTFs. Previously, G359.10–0.2 (the Snake) was the only NTF found south of the Galactic plane, though the Galactic center Radio Arc and Sgr C cross the plane. Thirteen of the 20 candidate NTFs are south of the Galactic plane.

The orientation of the NTFs is of particular interest because of their potential to discriminate between different NTF origin theories and for tracing GC magnetic fields. For the purposes of this discussion, orientation will be defined as the separation angle between the long axis of the NTF and the normal to the Galactic plane. The nine known isolated NTFs are, with the exception of G358.85+0.47, nearly normal to the Galactic plane. This observation supports the hypothesis that the magnetic field in the region is poloidal in nature (e.g., Morris & Serabyn 1996 and references therein). However, the new NTF population differs significantly, with a mean orientation of $35^\circ \pm 40^\circ$. Furthermore, NTFs much closer to the plane and to the GC than G358.85+0.47, such as NTF G359.22–0.16, are nearly parallel to the Galactic plane. This suggests that the GC magnetic field is significantly more complicated than a simple dipole. Though it is noteworthy that the brightest NTFs align normal to the plane, the new NTF population would appear to

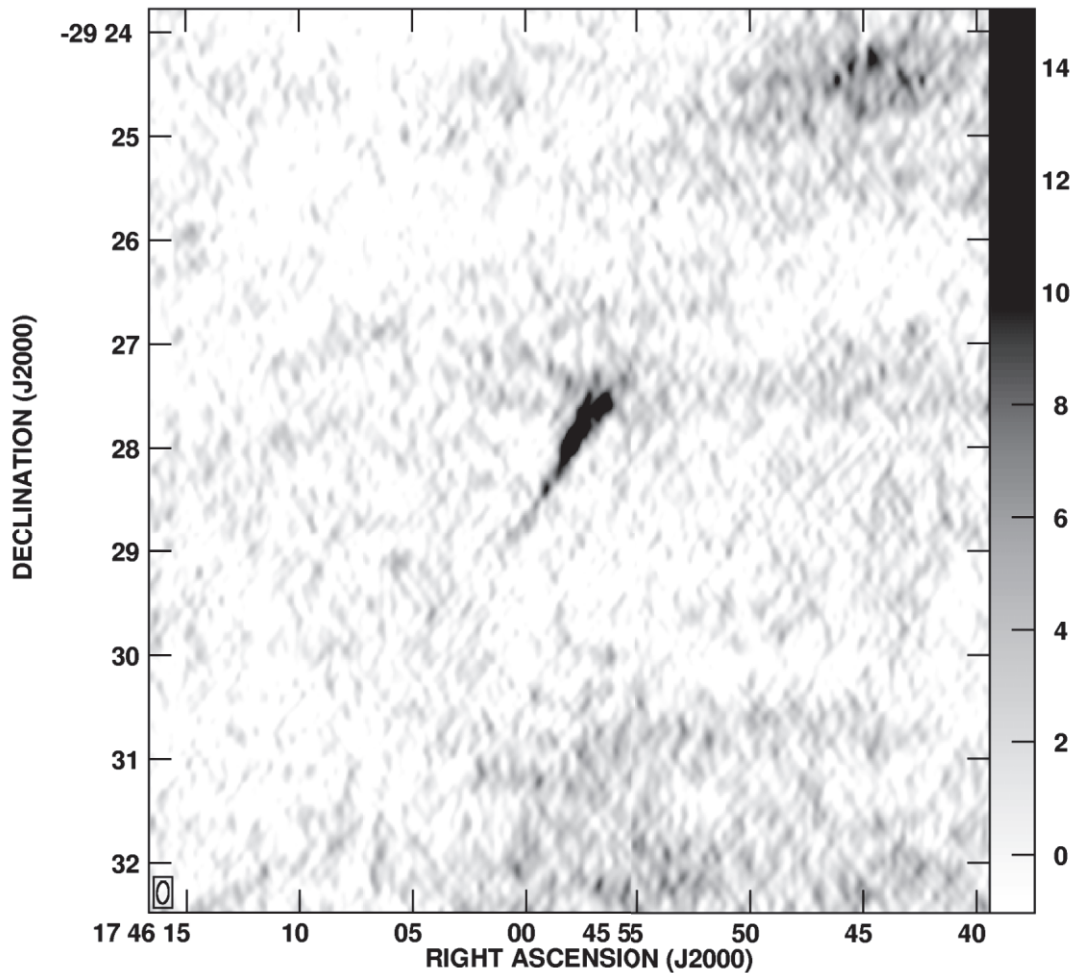


FIG. 19.—NTF candidate G359.59–0.34. The gray scale is linear between -1 and 15 mJy beam^{-1} . Primary-beam correction has not been applied; the value at the center of the field is 1.08 .

imply a larger scale nonpoloidal field or a disordered component of the magnetic field. Moreover, the pseudorandom orientation of weaker candidate NTFs may indicate a physical manifestation not directly connected to the properties of any global field.

6.1. NTFs and NTF Candidates

Candidates G359.86–0.24 and G359.66–0.11: Lying to the south of Sgr A in Figure 12, these long, low-brightness NTF candidates both curve northward.

Candidates G359.88–0.07 and G359.85–0.02: To the south and west of the supernova remnant Sgr A East in Figure 12, and separated by only $4'$, these NTF candidates are nearly perpendicular to each other. Candidate NTF G359.85–0.02 is in itself interesting in that it is so close to the plane and to the Galactic center yet is parallel to the plane. The simple dipole model of the GC magnetic field would be challenged to explain this NTF orientation. G359.85–0.02 was marginally detected at 620 MHz and labeled “Thread U” by Roy (2003), and G359.88–0.07 was identified by Lang et al. (1999) as a “streak.”

Candidates G0.02+0.04 and G0.06–0.07: To the north of Sgr A in Figure 12, these two faint NTF candidates are nearly parallel to the nearby bright filament G0.08+0.15. G0.02+0.04 was identified by Lang et al. (1999) as a “streak.”

Candidate G359.90+0.19: To the south of the western extension of G0.08+0.15, this NTF candidate differs in orientation

by roughly 35° from the nearby bright NTF. If this candidate is an NTF, it traces what must be a significant magnetic field gradient in this region.

NTF G359.10–0.2 (the Snake): G359.10–0.2 (Fig. 13) was reported by LaRosa et al. (2000) to have a length of $5.2'$. Reduced sensitivity to large-scale features and increased sensitivity to small-scale features in this image show that this feature in fact extends over more than $20'$, has a large “kink” in the middle, and shows curvature in different directions on each side of the kink—observations that are in agreement with higher frequency observations of this source (Gray et al. 1995).

Candidates G359.40–0.07 and G359.40–0.03: To the south of Sgr C in Figure 14 lies candidate NTF G359.40–0.07. This source was observed by Liszt & Spiker (1995) at 18 cm and detected as a small-diameter source in LaRosa et al. (2000). We derive a 20/90 cm spectral index of $\alpha \approx -0.1$. Higher resolution, 20 cm observations (Lazio & Cordes 2004) show the source to have a filamentary appearance.

Candidate NTF G359.40–0.03 may be a faint extension of G359.40–0.07. If one source, the bright part of is distinctly nonperpendicular to the Galactic plane, while the extension curves and becomes more perpendicular. This demonstrates a significant magnetic field gradient, particularly given its proximity to Sgr C, which does not.

Candidate G359.36+0.09: Figure 14 shows that this source lies just to the west of Sgr C. At high resolution, the western

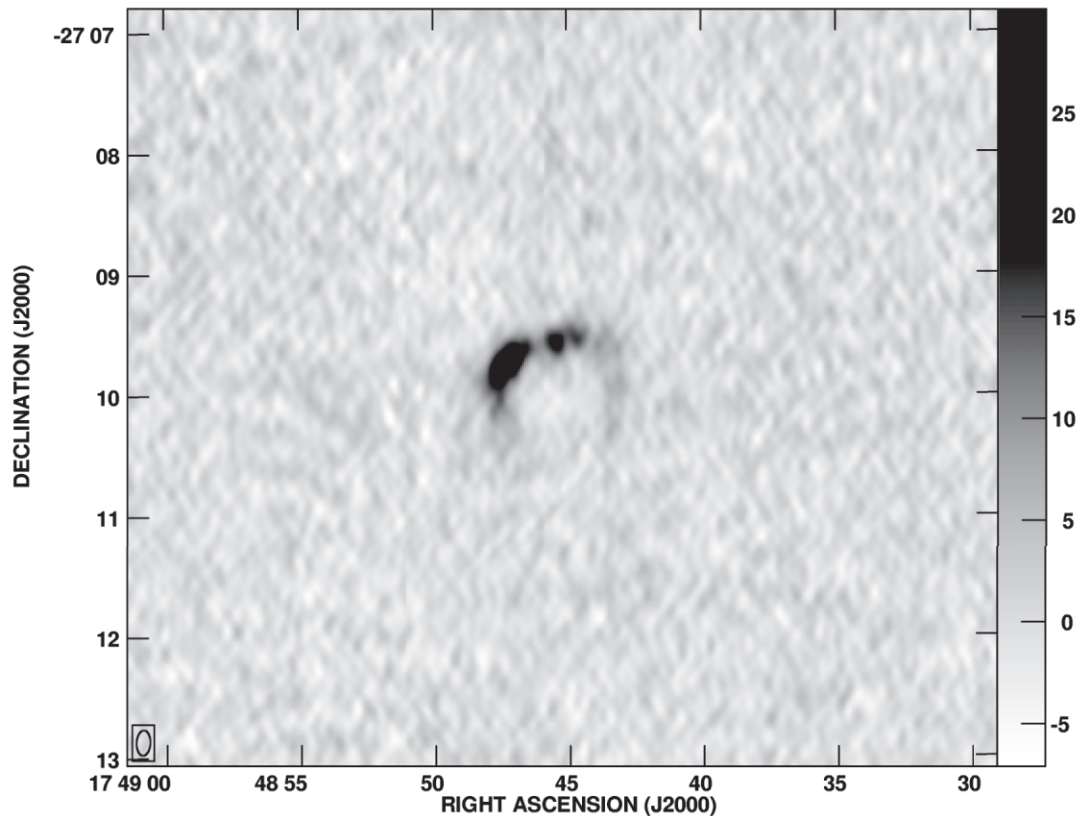


FIG. 20.—Supernova remnant G1.88+0.33. The gray scale is linear between -7 and 30 mJy beam^{-1} . Primary-beam correction has not been applied; the value at the center of the field is 5.01 .

end of the Sgr C filament is resolved into two distinct filaments (Liszt & Spiker 1995). The end of the Sgr C filament begins to flare and there is linear source G359.36+0.09, which may connect to the bottom filament of Sgr C. A very faint structure appears to cross this filament between it and Sgr C. If real, this would be the second example of interacting filaments in the Sgr C region, as G359.43+0.13 to the north also exhibits a crossing filament.

NTF G359.22–0.16: Figure 14 shows that this NTF lies to the south of the eastern part of Sgr C. This NTF has been observed to have a polarization of $\sim 40\%$ at 6 cm (LaRosa et al. 2004), confirming this source as an NTF. This NTF is nearly parallel to the Galactic plane, making it only the second confirmed NTF to be parallel to the plane, yet it is much closer to the plane than G358.85+0.47, “the Pelican,” the only other previously known parallel NTF. Furthermore, since the end of this source is less than 10 pc in projection from the Sgr C filament yet nearly normal to Sgr C, a simple dipole Galactic magnetic field structure cannot explain this filament.

Candidate G359.43+0.13: Figure 14 shows this candidate to lie northwest of Sgr C. This cross-shaped source may be an example of interacting NTFs. Even if this structure is simply a projection effect, we have another potential NTF that is parallel to the Galactic plane, and one that is far closer to Sgr A than is G358.85+0.47, the Pelican (Lang et al. 1999).

NTF G0.39–0.12 and candidates G0.37–0.07, G0.43+0.01, and G0.39+0.05: Figure 15 shows our candidates between Sgr B1 and the Radio Arc. They appear to be isolated NTFs that cross the plane with the same orientation as the bundled filaments in the Galactic center Radio Arc. NTF G0.39–0.12 has been observed to have a 6 cm polar-

ization greater than 10% (LaRosa et al. 2004) and is therefore confirmed as an NTF. These NTFs are the only known NTFs known north of the Radio Arc and therefore significantly increase the volume over which the NTF phenomenon occurs.

Candidate G359.12+0.66: Figure 16 shows the very faint G359.12+0.66. This filament was first detected at higher frequencies (M. Morris 2002, private communication) and is at the limits of detection here. This is a very long filament ($\sim 15.6'$) that is far above the Galactic plane and appears to bifurcate in the middle.

Candidate G359.33–0.42: Figure 17 shows the short G359.33–0.42. This candidate NTF is very nearly perpendicular to the Galactic plane, making it the only perpendicular candidate south of the plane.

Candidate G359.99–0.54: Figure 18 shows the very faint candidate NTF G359.99–0.54. Though no part of this filament has a flux density greater than 3 times the rms noise of the image, it is detectable by comparing the flux density of the region with nearby regions. This filament is the farthest south of the Galactic plane of all the NTFs.

Candidate G359.59–0.34: Figure 19 shows G359.59–0.34. This short candidate flares significantly to the northwest, more than tripling its width. Other NTFs are observed to flare, but this is the most extreme example.

6.2. SNR G1.88+0.33

Figure 20 shows supernova remnant G1.88+0.33. Considered a small-diameter source in LaRosa et al. (2000), it is now resolved in our image. First reported as an SNR by Green & Gull (1984), this remnant is quite small ($<1'$) and, if it could

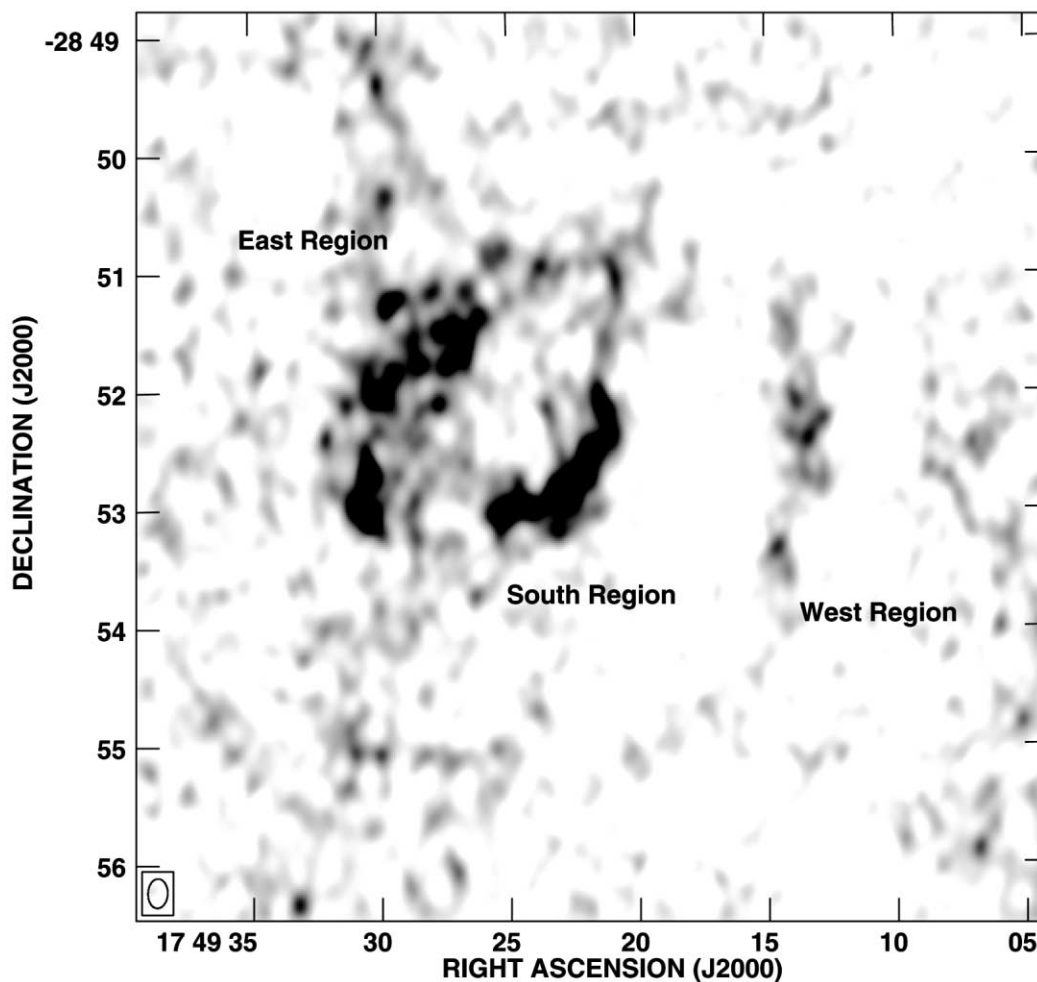


FIG. 21.—H II region G0.4–0.6. The gray scale is linear between 0 and 10 mJy beam^{−1}. Primary-beam correction has not been applied; the value at the center of the field is 1.28. The three regions indicated were used to determine spectral indices as described in § 6.3.

be shown to be nearby, would be one of the youngest known Galactic SNRs. A 327/74 MHz spectral index of approximately -0.65 (Brogan et al. 2004) indicates that the remnant does not have significant 74 MHz absorption. The fact that the line of sight passes within 2° of the Galactic center suggests that it may be on the near side of the GC to avoid absorption, but this is not a robust distance indicator. If indeed it is on this side of the GC (<7.8 kpc), it would be less than 3 pc in diameter, smaller than 428 year old Tycho (Schwarz et al. 1995).

6.3. G0.4–0.6

G0.4–0.6 is a moderately strong (1–2 Jy), extended ($\sim 5'$) region of emission, shown in Figure 21 and located approximately 1° east of the GC. Its morphology on the much lower resolution LaRosa et al. (2000) 330 MHz image consists of an incomplete spherical shell with a central component of emission, resembling a composite SNR. However, a comparison with an earlier VLA image at 1.6 GHz, kindly provided by H. Liszt, indicates that each of the source components shown in Figure 21 has a flat-to-inverted spectrum. VLA observations obtained by us in 2001 at 4.8 GHz, together with previous, lower resolution, single-dish measurements at 4.9 and 10 GHz (Altenhoff et al. 1979; Handa et al. 1987), demonstrate that the spectrum is flat at high frequencies.

An upper limit of only 1% polarization was determined from the recent 4.8 GHz observation. We consider unlikely

the possibility of severe depolarization due to a foreground thermal plasma. The morphology at 4.8 GHz suggests that the region of emission may actually consist of two physically distinct sources with one comprising the eastern and southern regions as indicated in the figure, and a second, separate western region.

Based on its spectrum and unpolarized emission, we conclude that G0.4–0.6 is most likely an H II region (or regions) with decreasing flux density below ~ 1 GHz as a result of self-absorption. This interpretation is supported by a single-dish observation (Downes et al. 1980) that detected H110a and H₂CO recombination lines from the region. Also, the radial velocity measurements of Downes et al. provide evidence that the source is located in the GC.

7. CONCLUSIONS

We have presented a high-resolution, high-sensitivity image of the Galactic center at 330 MHz. Synthesized from new observations and utilizing improved low-frequency data reduction procedures, this image improves on previous 330 MHz images of the GC (LaRosa et al. 2000) by roughly a factor of 5 in both resolution and surface brightness sensitivity.

In this image we have identified 241 small-diameter sources (diameters $\lesssim 15''$), tripling the number detected in previous low-frequency images of this region (LaRosa et al. 2000). Of these, roughly 40% can be identified with sources detected at

higher frequencies, primarily those in the 1.4 GHz GPSR catalog (Zoonematkermani et al. 1990; Helfand et al. 1992), enabling spectral index determinations. The spectral index distribution is broadly consistent with that expected from an extragalactic population of sources, though there are significant tails to both steep-spectrum and flat-spectrum sources. The remaining $\sim 60\%$ show clustering along the Galactic plane, and roughly 50% of this population have spectral index upper limits ($\alpha \leq -0.7$) that are inconsistent with extragalactic sources. The exact nature of these sources is unknown, but candidates include young SNRs, pulsars, and stellar wind shocks from young stellar objects, stellar clusters, or both. A paucity of low flux density small-diameter sources with respect to an extragalactic population is interpreted as the effect of a free electron scattering screen along the Galactic plane.

Of 14 known pulsars in the survey area, four are detected. Nondetections are explained through low intrinsic brightness at higher frequencies and/or positions far from the phase center of the observations. Thirty sources were classified as pulsar candidates based on morphology and spectrum.

We have identified 20 nonthermal filaments and NTF candidates. If all are eventually confirmed, the census of NTFs in the Galactic center will have tripled. The pseudorandom orientation of these filaments is in stark contrast to previously detected filaments, which with one exception are all nearly normal to the Galactic plane. As NTFs have been thought to be tracers of the Galactic center magnetic structure, the in-

troduction of randomly oriented filaments necessitates reexamination of the paradigm of a strong, ordered, global magnetic field, currently accepted theories of NTF formation, or both.

Future work will include a 330 MHz Galactic center image utilizing all VLA configurations in combination with data from the Green Bank Telescope, and 74 MHz VLA imaging of the Galactic center.

The original data request was written with the help of K. Anantharamaiah. "Anantha" passed away during the initial stages of this project and will be missed greatly. The authors would like to thank Mariana S. Lazarova and Jennifer L. Neureuther, students at Sweet Briar College, for their assistance in small-diameter source location and quantification. Basic research in radio astronomy at the NRL is supported by the Office of Naval Research. S. D. H. was supported by the Jeffres Memorial Trust and the Research Corporation. The National Radio Astronomy Observatory is a facility of the National Science Foundation operated under cooperative agreement by Associated Universities, Inc. This research has made use of the SIMBAD database, operated at CDS, Strasbourg, France. This research has also made use of the CATS database, maintained at the Special Astrophysical Observatory, Russia (Verkhodanov et al. 1997).

REFERENCES

- Altenhoff, W. J., Downes, D., Pauls, T., & Schraml, J. 1979, *A&AS*, 35, 23
- Anantharamaiah, K. R., Pedlar, A., Ekers, R. D., & Goss, W. M. 1991, *MNRAS*, 249, 262
- Baars, J. W. M., Genzel, R., Pauliny-Toth, I. I. K., & Witzel, A. 1977, *A&A*, 61, 99
- Becker, R. H., White, R. L., Helfand, D. J., & Zoonematkermani, S. 1994, *ApJS*, 91, 347
- Bower, G. C., Falcke, H., & Backer, D. C. 1999, *ApJ*, 523, L29
- Brogan, C. L., et al. 2004, in preparation
- Clark, D. H., & Stephenson, F. R. 1977, *The Historical Supernovae* (Oxford: Pergamon)
- Cohen, A. S., et al. 2003, *ApJ*, 591, 640
- Condon, J. J., Cotton, W. D., Greisen, E. W., Yin, Q. F., Perley, R. A., Taylor, G. B., & Broderick, J. J. 1998, *AJ*, 115, 1693
- Cordes, J. M., & Lazio, T. J. W. 1997, *ApJ*, 475, 557
- . 2003, preprint (astro-ph/0207156)
- Cornwell, T., & Fomalont, E. B. 1999, in *ASP Conf. Ser. 180, Synthesis Imaging in Radio Astronomy II*, ed. G. B. Taylor, C. L. Carilli, & R. A. Perley (San Francisco: ASP), 187
- Cornwell, T. J., & Perley, R. A. 1992, *A&A*, 261, 353
- De Brueck, C., van Breugel, W., Röttgering, H. J. A., & Miley, G. 2000, *A&AS*, 143, 303
- Downes, D., Wilson, T. L., Bieging, J., & Wink, J. 1980, *A&AS*, 40, 379
- Erickson, W. C. 1984, *J. Astrophys. Astron.*, 5, 55
- Frail, D. A., Diamond, P. J., Cordes, J. M., & van Langevelde, H. J. 1994, *ApJ*, 427, L43
- Gray, A. D., Nicholls, J., Ekers, R. D., & Cram, L. E. 1995, *ApJ*, 448, 164
- Green, D. A. 1991, *PASP*, 103, 209
- Green, D. A., & Gull, S. F. 1984, *Nature*, 312, 527
- Handa, T., Sofue, Y., Nakai, N., Hirabayashi, H., & Inoue, M. 1987, *PASJ*, 39, 709
- Helfand, D. J., Zoonematkermani, S., Becker, R. H., & White, R. L. 1992, *ApJS*, 80, 211
- Hjellming, R. M., Rupen, M. P., & Mioduszewski, A. J. 1998, *IAU Circ.* 6934
- Hyman, S. D., Lazio, T. J. W., Kassim, N. E., & Bartleson, A. L. 2002, *AJ*, 123, 1497
- Hyman, S. D., Lazio, T. J. W., Kassim, N. E., Nord, M. E., & Neureuther, J. L. 2003, *Astron. Nachr.*, 324(S1), 79
- Lang, C. C., Morris, M., & Echevarria, L. 1999, *ApJ*, 526, 727
- LaRosa, T. N., Kassim, N. E., Lazio, T. J. W., & Hyman, S. D. 2000, *AJ*, 119, 207 (erratum 119, 3145)
- LaRosa, T. N., Lazio, T. J. W., & Kassim, N. E. 2001, *ApJ*, 563, 163
- LaRosa, T. N., Nord, M. E., Lazio, T. J. W., & Kassim, N. E. 2004, *ApJ*, 607, 302
- Lazio, T. J. W., Anantharamaiah, K. R., Goss, W. M., Kassim, N. E., & Cordes, J. M. 1999, *ApJ*, 515, 196
- Lazio, T. J. W., & Cordes, J. M. 1998a, *ApJS*, 118, 201
- . 1998b, *ApJ*, 505, 715
- . 2004, in preparation
- Liszt, H. S., & Spiker, R. W. 1995, *ApJS*, 98, 259
- Lorimer, D. R., Yates, J. A., Lyne, A. G., & Gould, D. M. 1995, *MNRAS*, 273, 411
- Lyne, A. G., et al. 2004, *Science*, 303, 1153
- Manchester, R., Hobbs, G., Teoh, A., & Hobbs, M. 2004, in *IAU Symp. 218, Young Neutron Stars and Their Environments*, ed. F. Camilo & B. M. Gaensler (San Francisco: ASP), in press
- Morris, M., & Serabyn, E. 1996, *ARA&A*, 34, 645
- Nord, M. E., Lazio, T. J. W., Kassim, N. E., Goss, W. M., & Duric, N. 2004, *ApJ*, 601, L51
- Pedlar, A., Anantharamaiah, K. R., Ekers, R. D., Goss, W. M., van Gorkom, J. H., Schwarz, U. J., & Zhao, J.-H. 1989, *ApJ*, 342, 769
- Roy, S. 2003, Ph.D. thesis, Univ. Pune
- Schwarz, U. J., Goss, W. M., Kalberla, P. M., & Benaglia, P. 1995, *A&A*, 299, 193
- Shore, S. N., & LaRosa, T. N. 1999, *ApJ*, 521, 587
- Steer, D. G., Dewdney, P. E., & Ito, M. R. 1984, *A&A*, 137, 159
- Tammann, G. A., Löffler, W., & Schröder, A. 1994, *ApJS*, 92, 487
- Taylor, J. H., Manchester, R. N., & Lyne, A. G. 1993, *ApJS*, 88, 529
- van Langevelde, H. J., Frail, D. A., Cordes, J. M., & Diamond, P. J. 1992, *ApJ*, 396, 686
- Verkhodanov, O. V., Trushkin, S. A., Andernach, H., & Chernenkov, V. N. 1997, in *ASP Conf. Ser. 125, Astronomical Data Analysis Software and Systems VI*, ed. G. Hunt & H. E. Payne (San Francisco: ASP), 322
- Wieringa, M. H. 1991, Ph.D. thesis, Rijksuniv. Leiden
- Yusef-Zadeh, F., Nord, M., Wardle, M., Law, C., Lang, C., & Lazio, T. J. W. 2003, *ApJ*, 590, L103
- Zoonematkermani, S., Helfand, D. J., Becker, R. H., White, R. L., & Perley, R. A. 1990, *ApJS*, 74, 181